

1 Inhibitory control of shared variability in cortical networks

2 Marius Pachitariu^{*,1}, Carsen Stringer^{*,2}, Michael Okun¹, Peter Bartho³, Kenneth Harris¹, Peter Latham²,

3 Maneesh Sahani², Nicholas Lesica⁴

4 * equal contribution

5 ¹ Institute of Neurology, UCL, London, UK

6 ² Gatsby Computational Neuroscience Unit, UCL, London, UK

7 ³ Hungarian Academy of Sciences, Budapest, Hungary

8 ⁴ Ear Institute, UCL, London, UK

9 SUMMARY

10 Cortical networks exhibit intrinsic dynamics that drive coordinated, large-scale fluctuations across neuronal
11 populations and create noise correlations that impact sensory coding. To investigate the network-level
12 mechanisms that underlie these dynamics, we developed novel computational techniques to fit a determin-
13 istic spiking network model directly to multi-neuron recordings from different species, sensory modalities,
14 and behavioral states. The model accurately reproduced the wide variety of activity patterns in our record-
15 ings, and analysis of its parameters suggested that differences in noise correlations across recordings were
16 due primarily to differences in the strength of feedback inhibition. Further analysis of our recordings con-
17 firmed that putative inhibitory interneurons were indeed more active during desynchronized cortical states
18 with weak noise correlations. Our results demonstrate the power of fitting spiking network models directly to
19 multi-neuron recordings and suggest that inhibition modulates the interactions between intrinsic dynamics
20 and sensory inputs by controlling network stability.

21 **INTRODUCTION**

22 The patterns of cortical activity evoked by sensory stimuli provide the internal representation of the outside
23 world that underlies perception. However, these patterns are driven not only by sensory inputs, but also
24 by the intrinsic dynamics of the underlying cortical network. These dynamics can create correlations in the
25 activity of neuronal populations with important consequences for coding and computation [Shadlen et al.,
26 1996, Abbott and Dayan, 1999, Moreno-bote et al., 2014]. The correlations between pairs of neurons
27 have been studied extensively [Cohen and Kohn, 2011, Ecker et al., 2010, Averbeck et al., 2006] and
28 substantial effort has been directed toward understanding their origin [Renart et al., 2010]. Recent studies
29 have demonstrated that correlations are driven by dynamics involving coordinated, large-scale fluctuations
30 in the activity of many neurons [Sakata and Harris, 2009, Pachitariu et al., 2015, Okun et al., 2015] and,
31 importantly, that the nature of these dynamics and the correlations that they create are dependent on the
32 state of the underlying network; it has been shown that various factors modulate the strength of correlations,
33 such as anaesthesia [Harris and Thiele, 2011, Schölvicck et al., 2015, Constantinople and Bruno, 2011],
34 attention [Cohen and Maunsell, 2009, Mitchell et al., 2009, Buran et al., 2014], locomotion [Schneider et al.,
35 2014, Erisken et al., 2014], and alertness [Vinck et al., 2015, McGinley et al., 2015a]. In light of these
36 findings, it is critical that we develop a deeper understanding of the origin and consequences of correlations
37 at the biophysical network level.

38 In this study, we use a large number of multi-neuron recordings and a model-based analysis to investigate
39 the mechanisms that control noise correlations, a manifestation of intrinsic dynamics during sensory pro-
40 cessing in which the variability in responses to identical stimuli is shared between neurons. For our results to
41 provide direct insights into physiological mechanisms, we required a model with several properties: (1) the
42 model must be able to internally generate the complex intrinsic dynamics of cortical networks, (2) it must be
43 possible to fit the model parameters directly to spiking activity from individual multi-neuron recordings, and
44 (3) the model must be biophysically interpretable and enable predictions that can be tested experimentally.

45 Thus far, the only network models that have been fit directly to multi-neuron recordings have relied on either
46 abstract dynamical systems[[Curto et al., 2009](#)] or probabilistic frameworks in which variability is modelled
47 as stochastic and shared variability arises through abstract latent variables whose origin is assumed to lie
48 either in unspecified circuit processes [[Ecker et al., 2014](#), [Macke et al., 2011](#), [Pachitariu et al., 2013](#)] or else-
49 where in the brain [[Goris et al., 2014](#), [de la Rocha et al., 2007](#)]. While these models are able to accurately
50 reproduce many features of cortical activity and provide valuable summaries of the phenomenological and
51 computational properties of cortical networks, their parameters are difficult to interpret at a biophysical level.

52 One alternative to these abstract stochastic models is a biophysical spiking network, which can generate
53 variable neural activity through chaotic amplification of different initial conditions [[van Vreeswijk and Som-
54 polinsky, 1996](#), [Amit and Brunel, 1997](#), [Renart et al., 2010](#), [Litwin-Kumar and Doiron, 2012](#), [Wolf et al.,
55 2014](#)]. These networks can be designed to have interpretable parameters, but have not yet been fit directly
56 to multi-neuron recordings and, thus, their use has been limited to attempts to explain qualitative features of
57 cortical dynamics through manual tuning of network parameters. This approach has revealed a number of
58 different network features that are capable of controlling dynamics, such as clustered connectivity [[Litwin-
59 Kumar and Doiron, 2012](#)] or adaptation currents [[Latham et al., 2000](#), [Destexhe, 2009](#)], but the inability to fit
60 the networks directly to recordings has made it difficult to identify which of these features play an important
61 role in vivo. To overcome this limitation, we developed a novel computational approach that allowed us to
62 fit a spiking network directly to individual multi-neuron recordings. By taking advantage of the computa-
63 tional power of graphics processing units (GPUs), we were able to sample from the network with millions of
64 different parameter values to find those that best reproduced the activity in a given recording.

65 We verified that a network with intrinsic variability and a small number of parameters was able to capture the
66 apparently doubly chaotic structure of cortical activity [[Churchland and Abbott, 2012](#)] and accurately repro-
67 duce the range of different spiking patterns observed in vivo. Like classical excitatory-inhibitory networks,
68 the model generates deterministic microscopic trial-to-trial variability in the spike times of individual neu-
69 rons [[van Vreeswijk and Sompolinsky, 1996](#)], as well as macroscopic variability in the form of coordinated,

70 large-scale fluctuations that are shared across neurons. Because these fluctuations are of variable duration,
71 arise at random times, and do not necessarily phase-lock to external input, they create noise correlations in
72 evoked responses that match those observed *in vivo*.

73 To gain insight into the mechanisms that control noise correlations *in vivo*, we fit the network model to
74 recordings from different species, sensory modalities, and behavioral states. After verifying that the model
75 accurately captured the diversity of intrinsic dynamics in our recordings, we analyzed the parameters of the
76 model fit to each recording and found that differences in the strength of noise correlations across recordings
77 were reflected primarily in differences in the strength of feedback inhibition in the model. The importance of
78 inhibition was further supported by simulations demonstrating that strong inhibition is sufficient to stabilize
79 network dynamics and suppress noise correlations, as well as additional analysis of our recordings showing
80 that the activity of inhibitory interneurons is increased during desynchronized cortical states with weak noise
81 correlations in both awake and anesthetized animals.

82 RESULTS

83 Cortical networks exhibit a wide variety of intrinsic dynamics

84 To obtain a representative sample of cortical activity patterns, we made multi-neuron recordings from differ-
85 ent species (mouse, gerbil, or rat), sensory modalities (A1 or V1), and behavioral states (awake or under
86 one of several anesthetic agents). We compiled recordings from a total of 59 multi-neuron populations
87 across 6 unique recording types (i.e. species/modality/state combinations). The spontaneous activity in
88 different recordings exhibited striking differences not only in overall activity level, but also in the spatial and
89 temporal structure of activity patterns; while concerted, large-scale fluctuations were prominent in some
90 recordings, they were nearly absent in others (Figure 1A). In general, large-scale fluctuations were weak in
91 awake animals and strong under anesthesia, but this was not always the case (see summary statistics for
92 each recording in Figure S1 and further examples in Figure 3).

93 The magnitude and frequency of the large-scale fluctuations in each recording were reflected in the auto-
94 correlation function of the multi-unit activity (MUA, the summed spiking of all neurons in the population in
95 15 ms time bins). The autocorrelation function of the MUA decayed quickly to zero for recordings with weak
96 large-scale fluctuations, but had oscillations that decayed slowly for recordings with stronger fluctuations
97 (Figure 1B). The activity patterns in recordings with strong large-scale fluctuations were characterized by
98 clear transitions between up states, where most of the population was active, and down states, where the
99 entire population was silent. These up and down state dynamics were reflected in the distribution of the
100 MUA across time bins; recordings with strong large-scale fluctuations had a large percentage of time bins
101 with zero spikes (Figure 1C).

102 To summarize the statistical structure of the activity patterns in each recording, we measured four quantities.
103 We used mean spike rate to describe the overall level of activity, mean pairwise correlations to describe the
104 spatial structure of the activity patterns, and two different measures to describe the temporal structure of
105 the activity patterns - the decay time of the autocorrelation function of the MUA, and the percentage of MUA
106 time bins with zero spikes. While there were some dependencies in the values of these quantities across
107 different recordings (Figure 1D), there was also considerable scatter both within and across recording types.
108 This scatter suggests that there is no single dimension in the space of cortical dynamics along which the
109 overall level of activity and the spatial and temporal structure of the activity patterns all covary, but rather
110 that cortical dynamics span a multi-dimensional continuum [Harris and Thiele, 2011]. This was confirmed
111 by principal component analysis; even in the already reduced space described by our summary statistics,
112 three principal components were required to account for the differences in spike patterns across recordings
113 (Figure 1E).

114 **A deterministic spiking network model of cortical activity**

115 To investigate the network-level mechanisms that control cortical dynamics, we developed a biophysically-
116 interpretable model that was capable of reproducing the wide range of activity patterns observed in vivo.

117 We constructed a minimal deterministic network of excitatory spiking integrate-and-fire neurons with non-
118 selective feedback inhibition and single-neuron adaptation currents (Figure 2A). Each neuron receives con-
119 stant tonic input, and the neurons are connected randomly and sparsely with 5% probability. The neurons
120 are also coupled indirectly through global, supralinear inhibitory feedback driven by the spiking of the en-
121 tire network [Rubin et al., 2015], reflecting the near-complete interconnectivity between pyramidal cells and
122 interneurons in local populations [Hofer et al., 2011, Fino and Yuste, 2011, Packer and Yuste, 2011]. The
123 supralinearity of the inhibitory feedback is a critical feature of the network, as it shifts the balance of excitation
124 and inhibition in favor of inhibition when the network is strongly driven [Haider et al., 2013].

125 The model has five free parameters: three controlling the average strength of excitatory connectivity, the
126 strength of inhibitory feedback, and the strength of adaptation, respectively, and two controlling the strength
127 of the tonic input to each neuron, which is chosen from an exponential distribution. The timescales that
128 control the decay of the excitatory, inhibitory and adaptation currents are fixed at 5 ms, 3.75 ms and 375
129 ms, respectively. Note that no external noise input is required to generate variable activity; population-wide
130 fluctuations over hundreds of milliseconds are generated when the slow adaptation currents synchronize
131 across neurons to maintain a similar state of adaptation throughout the entire network, which, in turn, results
132 in coordinated spiking [Latham et al., 2000, Destexhe, 2009].

133 The variability in the model arises through chaotic amplification of small changes in initial conditions or small
134 perturbations to the network that cause independent simulations to differ dramatically. In some parameter
135 regimes, the instability of the network is such that the structure of the spike patterns generated by the model
136 is sensitive to changes in the spike times of individual neurons. In fact, a single spike added randomly to
137 a single neuron during simulated activity is capable of changing the time course of large-scale fluctuations,
138 in some cases triggering immediate population-wide spiking (Figure 2B, top rows). Variability of this nature
139 has been observed in vivo previously [London et al., 2010] and was also evident in our recordings when
140 comparing different extracts of cortical activity; spike patterns that were similar for several seconds often
141 began to differ almost immediately (Figure 2B, bottom rows).

142 **Multiple features of the network model can control its dynamics**

143 The dynamical regime of the network model is determined by the interactions between its different features.

144 To determine the degree to which each feature of the network was capable of influencing the structure of its

145 activity patterns, we analyzed the effects of varying the value of each model parameter. We started from a

146 fixed set of parameter values and simulated activity while independently sweeping each parameter between

147 the values that led to network silence and divergence. The results of these parameter sweeps clearly

148 demonstrate that each of the five parameters can exert strong control over the dynamics of the network, as

149 both the overall level of activity and the spatial and temporal structure of the patterns in simulated activity

150 varied widely with changes in each parameter (Figure 2C-D).

151 With the set of fixed parameter values used for the perturbation analysis, the network is in an unstable

152 regime with slow, ongoing fluctuations between up and down states. In this regime, the amplification of a

153 small perturbation results in a sustained, prolonged burst of activity (up state), which, in turn, drives a build-

154 up of adaptation currents that ultimately silences the network for hundreds of milliseconds (down state) until

155 the cycle repeats. These fluctuations can be suppressed when the network is stabilized by an increase in

156 the strength of feedback inhibition, which eliminates slow fluctuations and shifts the network into a regime

157 with weak, tonic spiking and weak correlations (Figure 2C-D, first column); in this regime, small perturbations

158 are immediately offset by the strong inhibition and activity is returned to baseline [Renart et al., 2010]. The

159 fluctuations between up and down states can also be suppressed by decreasing adaptation (Figure 2C-D,

160 second column); without adaptation currents to create slow, synchronous fluctuations across the network,

161 neurons exhibit strong, tonic spiking.

162 The stability of the network can also be influenced by changes in excitation or tonic input. Increasing

163 the strength of excitation results in increased activity and stronger fluctuations, as inhibition is unable to

164 compensate for the increased amplification of small perturbations by recurrent excitation (Figure 2C-D, third

165 column); in regimes with strong excitation, it is only the build-up of adaptation currents that prevents the

network from diverging. Increasing the spread or baseline level of tonic input also results in increased activity, but with suppression, rather than enhancement, of slow fluctuations (Figure 2C-D, fourth and fifth column). As either the spread or baseline level of tonic input is increased, more neurons begin to receive tonic input that is sufficient to overcome their adaptation current and, thus, begin to quickly reinitiate up states after only brief down states and, eventually, transition to tonic spiking.

171 The network model reproduces the dynamics observed in vivo

The network simulations demonstrate that each of its features is capable of controlling its dynamics and shaping the structure of its activity patterns. To gain insight into the mechanisms that may be responsible for creating the differences in dynamics observed in vivo, we fit the model to each of our recordings. We optimized the model parameters so that the patterns of activity generated by the network matched those observed in spontaneous activity (Figure 3A). We measured the agreement between the simulated and recorded activity by a cost function which was the sum of discrepancies in the autocorrelation function of the MUA, the distribution of MUA values across time bins, and the mean pairwise correlations. Together, these statistics describe the overall level of activity in each recording, as well as the spatial and temporal structure of its activity patterns. We ensured that the optimal model parameters were uniquely identified by using a cost function that captures many different properties of the recorded activity while fitting only a very small number of model parameters [Marder et al., 2015].

Fitting the model to the recordings required us to develop new computational techniques. The network parametrization is fundamentally nonlinear, and the statistics used in the cost function are themselves nonlinear functions of a dynamical system with discontinuous integrate-and-fire mechanisms. Thus, as no gradient information was available to guide the optimization, we used Monte Carlo simulations to generate activity and measure the relevant statistics with different parameter values. By using GPU computing resources, we were able to design and implement network simulations that ran 10000x faster than real time, making it feasible to sample the cost function with high resolution and identify the parameter configuration

190 that resulted in activity patterns that best matched those of each recorded population.

191 The model was flexible enough to capture the wide variety of activity patterns observed across our record-
192 ings, producing both decorrelated, tonic spiking and coordinated, large-scale fluctuations between up and
193 down states as needed (see examples in Figure 3B, statistics for all recordings and models in Figure S1,
194 and parameter values and goodness-of-fit measures for all recordings in Figure S2). To our knowledge, this
195 is the first time that the parameters of a spiking neural network have been fit directly to the spiking activity in
196 multi-neuron recordings.

197 **Strong inhibition suppresses noise correlations**

198 Our main interest was in understanding how the different network-level mechanisms that are capable of
199 controlling intrinsic dynamics contribute to the shared variability in responses evoked by sensory stimuli.
200 The wide variety of intrinsic dynamics in our recordings was reflected in the differences in evoked responses
201 across recording types; while some populations responded to the onset of a stimulus with strong, reliable
202 spiking events, the responses of other populations were highly variable across trials (Figure 4A). There
203 were also large differences in the extent to which the variability in evoked responses was shared across the
204 neurons in a population; pairwise noise correlations were large in some recordings and extremely weak in
205 others, even when firing rates were similar (Figure 4B).

206 Because evoked spike patterns can depend strongly on the specifics of the sensory stimulus, we could not
207 make direct comparisons between experimental responses across different species and modalities; our goal
208 was to identify the internal mechanisms that are responsible for the differences in noise correlations across
209 recordings and, thus, any differences in spike patterns due to differences in external input would confound
210 our analysis. To overcome this confound and compare evoked responses across recording types, we sim-
211 ulated the response of the network to the same external input for all recording types. We constructed the
212 external input using recordings of responses from more than 500 neurons in the inferior colliculus (IC), the

213 primary relay nucleus of the auditory midbrain that provides the main input to the thalamocortical circuit. We
214 have shown previously that the Fano factors of the responses of IC neurons to speech are close to 1 and the
215 noise correlations between neurons are extremely weak [Belliveau et al., 2014], suggesting that the spiking
216 activity of a population of IC neurons can be well described by series of independent, inhomogeneous Pois-
217 son processes. To generate the responses of each model network to the external input, we grouped the IC
218 neurons by their preferred frequency and selected a randomly chosen subset of 10 neurons from the same
219 frequency group to drive each cortical neuron (Figure 4C-D). Using the subset of our cortical recordings in
220 which we presented speech sounds that were also presented during the IC recordings, we verified that the
221 noise correlations in the simulated cortical responses were similar to those in the recordings (Figures 4E).

222 The parameter sweeps described in figure 2 demonstrated that there are multiple features of the model
223 network that can control its intrinsic dynamics, and a similar analysis of the noise correlations in simulated
224 responses to the IC input produced similar results (Figure S3). To gain insight into which of these features
225 could account for the differences in noise correlations across our recordings, we examined the dependence
226 of the strength of the noise correlations in each recording on each of the model parameters. While several
227 parameters were able to explain a significant amount of the variance in noise correlations across popula-
228 tions, the amount of variance explained by the strength of inhibitory feedback was by far the largest (Figure
229 5A). We also performed parameter sweeps to confirm that varying only the strength of inhibition was suf-
230 ficient to result in large changes in noise correlations in the dynamical regime of each recording (Figure
231 5B).

232 **Strong inhibition sharpens tuning and enables accurate decoding**

233 We also examined how different features of the network controlled other aspects of evoked responses. We
234 began by examining the extent to which differences in the value of each model parameter could explain
235 differences in receptive field size across recordings. To estimate receptive field size, we drove the model
236 network that was fit to each cortical recording with external inputs constructed from IC responses to tones,

237 and used the simulated responses to measure the width of the frequency tuning curves of each model
238 neuron. Although each model network received the same external inputs, the selectivity of the neurons in
239 the different networks varied widely. The average tuning width of the neurons in each network varied most
240 strongly with the strength of the inhibitory feedback in the network (Figure 5C), and varying the strength of
241 inhibition alone was sufficient to drive large changes in tuning width (Figure 5D). These results are consistent
242 with experiments demonstrating that inhibition can control the selectivity of cortical neurons [Lee et al.,
243 2012], but suggest that this control does not require structured lateral inhibition.

244 We also investigated the degree to which the activity patterns generated by the model fit to each cortical
245 recording could be used to discriminate different external inputs. We trained a decoder to infer which of
246 seven possible speech tokens evoked a given single-trial activity pattern and examined the extent to which
247 differences in the value of each model parameter could account for the differences in decoder performance
248 across populations. Again, the amount of variance explained by the strength of inhibitory feedback was by far
249 the largest (Figure 5E); decoding was most accurate for activity patterns generated by networks with strong
250 inhibition, consistent with the weak noise correlations and high selectivity of these networks. Parameter
251 sweeps confirmed that varying only the strength of inhibition was sufficient to result in large changes in
252 decoder performance (Figure 5F).

253 **Activity of fast-spiking (FS) neurons is increased during periods of cortical desynchronization with
254 weak noise correlations**

255 Our model-based analyses suggest an important role for feedback inhibition in controlling the way in which
256 responses to sensory inputs are shaped by intrinsic dynamics. In particular, our results predict that in-
257 hibition should be strong in dynamical regimes with weak noise correlations. To test this prediction, we
258 performed further analysis of our recordings to estimate the strength of inhibition in each population. We
259 classified the neurons in each recording based on the width of their spike waveforms (Figure S4); the wave-
260 forms fell into two distinct clusters, allowing us to separate fast-spiking (FS) neurons, which are mostly

261 parvalbumin-positive (PV+) inhibitory interneurons, from regular-spiking (RS) neurons, which are mostly ex-
262 citatory pyramidal neurons [Barthó et al., 2004, Madisen et al., 2012, Roux and Buzsáki, 2015, Cardin et al.,
263 2009].

264 Given the results of our model-based analyses, we hypothesized that the overall level of activity of FS
265 neurons should vary inversely with the strength of noise correlations. To identify sets of trials in each
266 recording that were likely to have either strong or weak noise correlations, we measured the level of cortical
267 synchronization. Previous studies have shown that noise correlations are strong when the cortex is in
268 a synchronized state, where activity is dominated by concerted, large-scale fluctuations, and weak when
269 the cortex is in a desynchronized state, where these fluctuations are suppressed [Pachitariu et al., 2015,
270 Schölvicck et al., 2015].

271 We began by analyzing our recordings from V1 of awake mice. We classified the cortical state during each
272 stimulus presentation based on the ratio of low-frequency LFP power to high-frequency LFP power [Sakata
273 and Harris, 2012] and compared evoked responses across the most synchronized and desynchronized
274 subsets of trials (Figure 6A). As expected, noise correlations were generally stronger during synchronized
275 trials than during desynchronized trials, and this variation in noise correlations with cortical synchrony was
276 evident both within individual recordings and across animals (Figure 6B-C). As predicted by our model-
277 based analyses, the change in noise correlations with cortical synchrony was accompanied by a change in
278 FS activity; there was a four-fold increase in the mean spike rate of FS neurons from the most synchronized
279 trials to the most desynchronized trials, while RS activity remained constant (Figure 6D-F).

280 We next examined our recordings from gerbil A1 under urethane in which the cortex exhibited transitions
281 between distinct, sustained synchronized and desynchronized states (Figure 6G). As in our awake record-
282 ings, cortical desynchronization under urethane was accompanied by a decrease in noise correlations and
283 an increase in FS activity (Figures 6I-K). In fact, both FS and RS activity increased with cortical desynchro-
284 nization under urethane, but the increase in FS activity was much larger.

285 Finally, we examined our remaining recordings from gerbil A1 under either ketamine/xylazine (KX) or fen-
286 tanyl/mebetomidine/midazolam (FMM) anesthesia. In these recordings, the cortex did not transition between
287 different dynamical regimes, so we could not track changes in noise correlations and FS activity within indi-
288 vidual populations. However, recordings under KX and FMM exhibited stable states with high and low noise
289 correlations respectively [Pachitariu et al., 2015] (Figure 7A), so we were able to make comparisons across
290 recordings. Noise correlations under FMM were extremely weak, while those under KX were the largest
291 in any of our recordings, so we expected FS activity under FMM to be much higher than that under KX.
292 Surprisingly, our initial analysis suggested the opposite; the average spike rate of FS neurons under KX was
293 larger than that under FMM (Figure 7B). Further analysis revealed, however, that there were many fewer
294 FS neurons in our KX populations than in our FMM populations (Figure 7C; all recordings were made in
295 the same region of gerbil A1 with the same multi-tetrode arrays, so a similar number of FS neurons should
296 be expected). The lack of FS neurons in our KX recordings suggests that inhibition under KX is so weak
297 that many FS cells become completely silent. When we measured FS activity as the sum of all spiking in
298 each population rather than the average spike rate of each neuron, the amount of FS activity was indeed
299 much larger under FMM than under KX, consistent with our observations in other recording types and the
300 predictions of our model-based analyses (Figure 7D-E).

301 **DISCUSSION**

302 We have shown that a deterministic spiking network model is capable of reproducing the wide variety of
303 multi-neuron cortical activity patterns observed in vivo. Through chaotic amplification of small perturbations,
304 the model generates activity with both trial-to-trial variability in the spike times of individual neurons and
305 coordinated, large-scale fluctuations of the entire network. Although several features of the model network
306 are capable of controlling its intrinsic dynamics, our analysis suggests that the differences in the shared
307 variability in evoked responses across our in vivo recordings can be accounted for by differences in feedback
308 inhibition. When we fit the model to each of our individual recordings, we found that noise correlations, as

309 well as stimulus selectivity and decoding accuracy, varied strongly with the strength of inhibition in the
310 network. We also found that the activity of fast-spiking neurons in our recordings was increased during
311 periods of cortical desynchronization with weak noise correlations. Taken together, these results suggest
312 that the control of network stability by inhibition plays a critical role in modulating the impact of intrinsic
313 cortical dynamics on sensory responses.

314 **Inhibition controls the strength of the large-scale fluctuations that drive noise correlations**

315 Our results are consistent with experiments showing that one global dimension of variability largely explains
316 both the pairwise correlations between neurons [Okun et al., 2015] and the time course of population ac-
317 tivity [Ecker et al., 2014]. In our network model, the coordinated, large-scale fluctuations that underlie this
318 global dimension of variability are generated primarily by the interaction between recurrent excitation and
319 adaptation. When inhibition is weak, small deviations from the mean spike rate can be amplified by strong,
320 non-specific, recurrent excitation into population-wide events (up states). These events produce strong
321 adaptation currents in each activated neuron, which, in turn, result in periods of reduced spiking (down
322 states) [Latham et al., 2000, Destexhe, 2009, Curto et al., 2009, Mochol et al., 2015]. The alternations
323 between up states and down states have an intrinsic periodicity given by the timescale of the adaptation
324 currents, but the chaotic nature of the network adds an apparent randomness to the timing of individual
325 events, thus creating intrinsic temporal variability.

326 The intrinsic temporal variability in the network imposes a history dependence on evoked responses; be-
327 cause of the build-up of adaptation currents during each spiking event, external inputs arriving shortly after
328 an up state will generally result in many fewer spikes than those arriving during a down state [Curto et al.,
329 2009]. This history dependence creates a trial-to-trial variability in the total number of stimulus-evoked
330 spikes that is propagated and reinforced across consecutive stimulus presentations to create noise corre-
331 lations. However, when the strength of the inhibition in the network is increased, the inhibitory feedback is
332 able to suppress some of the amplification by the recurrent excitation, and the transitions between clear up

333 and down states are replaced by weaker fluctuations of spike rate that vary more smoothly over time. If the
334 strength of the inhibition is increased even further, such that it becomes sufficient to counteract the effects
335 of the recurrent excitation entirely, then the large-scale fluctuations in the network disappear, weakening the
336 history dependence of evoked responses and eliminating noise correlations.

337 **Global inhibition sharpens tuning curves and enables accurate decoding by stabilizing network dy-**
338 **namics**

339 Numerous experiments have demonstrated that inhibition can shape the tuning curves of cortical neurons,
340 with stronger inhibition generally resulting in sharper tuning [Isaacson and Scanziani, 2011]. The mecha-
341 nisms involved are still a subject of debate, but this sharpening is often thought to result from structured
342 connectivity that produces differences in the tuning of the excitatory and inhibitory synaptic inputs to individ-
343 ual neurons; lateral inhibition, for example, can sharpen tuning when neurons with similar, but not identical,
344 tuning properties inhibit each other. Our results, however, demonstrate that strong inhibition can sharpen
345 tuning in a network without any structured connectivity simply by controlling its dynamics.

346 In our model, broad tuning curves result from the over-excitability of the network. When inhibition is weak,
347 every external input will eventually excite every neuron in the network because those neurons that receive
348 the input directly will relay indirect excitation to the rest of the network. When inhibition is strong, however,
349 the indirect excitation is largely suppressed, allowing each neuron to respond selectively to only those
350 external inputs that it receives either directly or from one of the few other neurons to which it is strongly
351 coupled. Thus, when inhibition is weak and the network is unstable, different external inputs will trigger
352 similar population-wide events [Bathellier et al., 2012], so the selectivity of the network in this regime is
353 weak and its ability to encode differences between sensory stimuli is poor. In contrast, when inhibition is
354 strong and the network is stable, different external inputs will reliably drive different subsets of neurons, and
355 the activity patterns in the network will encode different stimuli with high selectivity and enable accurate
356 decoding.

357 **Experimental evidence for inhibitory stabilization of cortical dynamics**

358 The results of several previous experimental studies also support the idea that strong inhibition can sta-
359 bilize cortical networks and enhance sensory coding. In vitro studies have shown that pharmacologically
360 reducing inhibition in S1 increases the strength of the correlations between excitatory cells in a graded man-
361 ner [Sippy and Yuste, 2013]. In vivo whole-cell recordings in V1 of awake animals have demonstrated that
362 the stimulus-evoked inhibitory conductance is much larger than the corresponding excitatory conductance
363 [Haider et al., 2013]. This strong inhibition in awake animals quickly shunts the excitatory drive and results in
364 sharper tuning and sparser firing than the balanced excitatory and inhibitory conductances observed under
365 anesthesia. While some of the increased inhibition in awake animals may be due to inputs from other brain
366 areas [Yu et al., 2015], the increased activity of local inhibitory interneurons appears to play an important
367 role [Schneider et al., 2014, Kato et al., 2013]. However, not all studies have observed increased inhibition
368 in behaving animals [Zhou et al., 2014], and the effects of behavioral state on different inhibitory interneuron
369 types are still being investigated [Gentet et al., 2010, Gentet et al., 2012, Polack et al., 2013].

370 The effects of local inhibition on sensory coding have been tested directly using optogenetics. While the
371 exact roles played by different inhibitory neuron types are still under debate [Lee et al., 2014], the activation
372 of inhibitory interneurons generally results in sharper tuning and enhanced behavioral performance [Wilson
373 et al., 2012, Lee et al., 2012], while suppression of inhibitory interneurons has the opposite effect, decreas-
374 ing the signal-to-noise ratio and reliability of evoked responses across trials [Zhu et al., 2015]. These results
375 demonstrate that increased inhibition enhances sensory processing and are consistent with the overall sup-
376 pression of cortical activity that is often observed during active behaviors [Otazu et al., 2009, Schneider
377 et al., 2014, Kuchibhotla et al., 2016, Buran et al., 2014]. In fact, one recent study found that the best
378 performance in a detection task was observed on trials in which the pre-stimulus membrane voltage was
379 hyperpolarized and low-frequency fluctuations were absent [McGinley et al., 2015a], consistent with a sup-
380 pressed, inhibition-stabilized network state.

381 **Two different dynamical regimes with weak noise correlations**

382 A number of studies have observed that the noise correlations in cortical networks can be extremely weak
383 under certain conditions [Ecker et al., 2010, Renart et al., 2010, Hansen et al., 2012, Pachitariu et al., 2015].
384 It was originally suggested that noise correlations were weak because the network was in an asynchronous
385 state in which neurons are continuously depolarized with a resting potential close to the spiking thresh-
386 old [Renart et al., 2010, van Vreeswijk and Sompolinsky, 1996]. Experimental support for this classical
387 asynchronous state has been provided by intracellular recordings showing that the membrane potential of
388 cortical neurons is increased during locomotion [McGinley et al., 2015a] and hyper-arousal [Constantinople
389 and Bruno, 2011], resulting in tonic spiking. However, other experiments have shown that the membrane
390 potential of cortical neurons in behaving animals can also be strongly hyperpolarized with clear fluctuations
391 between up and down states [Sachidhanandam et al., 2013, Tan et al., 2014, McGinley et al., 2015a, Polack
392 et al., 2013].

393 These apparently conflicting results suggest that there may be multiple dynamical regimes in behaving an-
394 imals that are capable of producing weak noise correlations. There is mounting evidence suggesting that
395 different forms of arousal may have distinct effects on neural activity [McGinley et al., 2015b]. While most
396 forms of arousal tend to reduce the power of low-frequency fluctuations in membrane potential [Bennett
397 et al., 2013, Polack et al., 2013, McGinley et al., 2015a], locomotion tends to cause a persistent depolar-
398 ization of cortical neurons and drive tonic spiking, while task-engagement in stationary animals is generally
399 associated with hyperpolarization and weak activity [Vinck et al., 2015, Polack et al., 2013, McGinley et al.,
400 2015a, Otazu et al., 2009, Buran et al., 2014]. The existence of two different dynamical regimes with weak
401 noise correlations was also apparent in our recordings; while some recordings with weak noise correlations
402 resembled the classical asynchronous state with spontaneous activity consisting of strong, tonic spiking
403 (e.g. desynchronized urethane recordings and some awake recordings), other recordings with weak noise
404 correlations had relatively low spontaneous activity with clear, albeit weak, up and down states (e.g. FMM
405 recordings and other awake recordings). Our model was able to accurately reproduce spontaneous activity

406 patterns and generate evoked responses with weak noise correlations in both of these distinct regimes.

407 In addition to strong inhibition, the classical asynchronous state with strong, tonic spiking appears to require
408 a combination of weak adaptation and an increase in the number of neurons receiving strong tonic input (see
409 parameter sweeps in Figures 2C-D and parameter values for awake mouse V1 recordings in Figure S2).
410 Since large-scale fluctuations arise from the synchronization of adaptation currents across the population,
411 reducing the strength of adaptation diminishes the fluctuations [Destexhe, 2009, Curto et al., 2009, Mochol
412 et al., 2015]. Increasing tonic input also diminishes large-scale fluctuations, but in a different way [Latham
413 et al., 2000]; when a subset of neurons receive increased tonic input, their adaptation currents may no
414 longer be sufficient to silence them for prolonged periods, and the activity of these cells during what would
415 otherwise be a down state prevents the entire population from synchronizing. When the network in the
416 asynchronous state is driven by an external input, it responds reliably and selectively to different inputs.
417 Because the fluctuations in the network are suppressed and its overall level of activity remains relatively
418 constant, every input arrives with the network in the same moderately-adapted state, so there is no history
419 dependence to create noise correlations in evoked responses.

420 Unlike in the classical asynchronous state, networks in the hyperpolarized state have slow fluctuations in
421 their spontaneous activity, and the suppression of noise correlations in their evoked responses is dependent
422 on different mechanisms (see parameter values for gerbil A1 FMM recordings in Figure S2). The fluctuations
423 in the hyperpolarized network are only suppressed when the network is driven by external input. In our
424 model, this suppression of the shared variability in evoked responses is caused by the supralinearity of
425 the feedback inhibition [Rubin et al., 2015]. The level of spontaneous activity driven by the tonic input to
426 each neuron results in feedback inhibition with a relatively low gain, which is insufficient to overcome the
427 instability created by recurrent excitation. However, when the network is strongly driven by external input,
428 the increased activity results in feedback inhibition with a much higher gain, which stabilizes the network
429 and allows it to respond reliably and selectively to different inputs. This increase in the inhibitory gain of
430 the driven network provides a possible mechanistic explanation for the recent observation that the onset of

431 a stimulus quenches variability [Churchland et al., 2010] and switches the cortex from a synchronized to a
432 desynchronized state [Tan et al., 2014].

433 **Neuromodulators and inhibitory control of cortical dynamics**

434 Neuromodulators can exert a strong influence on cortical dynamics by regulating the balance of excita-
435 tion and inhibition in the network. While the exact mechanisms by which neuromodulators control cortical
436 dynamics are not clear, several lines of evidence suggest that neuromodulator release serves to enhance
437 sensory processing by increasing inhibition. Increases in acetylcholine (ACh) and norepinephrine (NE) have
438 been observed during wakefulness and arousal [Berridge and Waterhouse, 2003, Jones, 2008], and dur-
439 ing periods of cortical desynchronization in which slow fluctuations in the LFP are suppressed [Goad and
440 Dan, 2009, Chen et al., 2015, Castro-Alamancos and Gulati, 2014]. Stimulation of the basal forebrain has
441 been shown to produce ACh-mediated increases in the activity of fast-spiking neurons and decrease the
442 variability of evoked responses in cortex [Sakata, 2016, Castro-Alamancos and Gulati, 2014, Goad and
443 Dan, 2009]. In addition, optogenetic activation of cholinergic projections to cortex resulted in increased
444 firing of SOM+ inhibitory neurons and reduced slow fluctuations [Chen et al., 2015]. The release of NE in
445 cortex through microdialysis had similar effects, increasing fast-spiking activity and reducing spontaneous
446 spike rates [Castro-Alamancos and Gulati, 2014], while blocking NE receptors strengthened slow fluctua-
447 tions in membrane potential [Constantinople and Bruno, 2011]. More studies are needed to tease apart
448 the effects of different neurotransmitters on pyramidal cells and interneurons [Castro-Alamancos and Gulati,
449 2014, Chen et al., 2015, Sakata, 2016], but most of the existing evidence is consistent with our results in
450 suggesting that neuromodulators serve to suppress intrinsic fluctuations and enhance sensory processing
451 in cortical networks by increasing inhibition.

452 **References**

- 453 [Abbott and Dayan, 1999] Abbott, L. F. and Dayan, P. (1999). The effect of correlated variability on the
454 accuracy of a population code. *Neural Computation*, 11(1):91–101.
- 455 [Amit and Brunel, 1997] Amit, D. J. and Brunel, N. (1997). Model of global spontaneous activity and local
456 structured activity during delay periods in the cerebral cortex. *Cerebral Cortex*, 7(3):237–252.
- 457 [Averbeck et al., 2006] Averbeck, B. B., Latham, P. E., and Pouget, A. (2006). Neural correlations, popula-
458 tion coding and computation. *Nature Reviews Neuroscience*, 7(5):358–366.
- 459 [Barthó et al., 2004] Barthó, P., Hirase, H., Monconduit, L., Zugaro, M., Harris, K. D., and Buzsáki, G.
460 (2004). Characterization of neocortical principal cells and interneurons by network interactions and extra-
461 cellular features. *Journal of neurophysiology*, 92(1):600–608.
- 462 [Bathellier et al., 2012] Bathellier, B., Ushakova, L., and Rumpel, S. (2012). Discrete neocortical dynamics
463 predict behavioral categorization of sounds. *Neuron*, 76(2):435–449.
- 464 [Belliveau et al., 2014] Belliveau, L. A., Lyamzin, D. R., and Lesica, N. A. (2014). The neural representation
465 of interaural time differences in gerbils is transformed from midbrain to cortex. *The Journal of Neuro-
466 science*, 34(50):16796–16808.
- 467 [Bennett et al., 2013] Bennett, C., Arroyo, S., and Hestrin, S. (2013). Subthreshold mechanisms underlying
468 state-dependent modulation of visual responses. *Neuron*, 80(2):350–357.
- 469 [Berridge and Waterhouse, 2003] Berridge, C. W. and Waterhouse, B. D. (2003). The locus coeruleus-
470 noradrenergic system: Modulation of behavioral state and state-dependent cognitive processes. *Brain
471 Research Reviews*, 42(1):33–84.
- 472 [Buran et al., 2014] Buran, B. N., von Trapp, G., and Sanes, D. H. (2014). Behaviorally gated reduction of
473 spontaneous discharge can improve detection thresholds in auditory cortex. *The Journal of Neuroscience*,
474 34(11):4076–4081.

- 475 [Cardin et al., 2009] Cardin, J. A., Carlén, M., Meletis, K., Knoblich, U., Zhang, F., Deisseroth, K., Tsai,
476 L.-H., and Moore, C. I. (2009). Driving fast-spiking cells induces gamma rhythm and controls sensory
477 responses. *Nature*, 459(7247):663–667.
- 478 [Castro-Alamancos and Gulati, 2014] Castro-Alamancos, M. A. and Gulati, T. (2014). Neuromodulators
479 produce distinct activated states in neocortex. *The Journal of Neuroscience*, 34(37):12353–12367.
- 480 [Chen et al., 2015] Chen, N., Sugihara, H., and Sur, M. (2015). An acetylcholine-activated microcircuit
481 drives temporal dynamics of cortical activity. *Nature Neuroscience*, 18(6):892–902.
- 482 [Churchland and Abbott, 2012] Churchland, M. M. and Abbott, L. F. (2012). Two layers of neural variability.
483 *Nature Neuroscience*, 15(11):1472–1474.
- 484 [Churchland et al., 2010] Churchland, M. M., Yu, B. M., Cunningham, J. P., Sugrue, L. P., Cohen, M. R.,
485 Corrado, G. S., Newsome, W. T., Clark, A. M., Hosseini, P., Scott, B. B., Bradley, D. C., Smith, M. a.,
486 Kohn, A., Movshon, J. A., Armstrong, K. M., Moore, T., Chang, S. W., Snyder, L. H., Lisberger, S. G.,
487 Priebe, N. J., Finn, I. M., Ferster, D., Ryu, S. I., Santhanam, G., Sahani, M., and Shenoy, K. V. (2010).
488 Stimulus onset quenches neural variability: a widespread cortical phenomenon. *Nature Neuroscience*,
489 13(3):369–378.
- 490 [Cohen and Kohn, 2011] Cohen, M. R. and Kohn, A. (2011). Measuring and interpreting neuronal correla-
491 tions. *Nature Neuroscience*, 14(7):811–819.
- 492 [Cohen and Maunsell, 2009] Cohen, M. R. and Maunsell, J. H. R. (2009). Attention improves performance
493 primarily by reducing interneuronal correlations. *Nature Neuroscience*, 12(12):1594–1600.
- 494 [Constantinople and Bruno, 2011] Constantinople, C. M. and Bruno, R. M. (2011). Effects and mechanisms
495 of wakefulness on local cortical networks. *Neuron*, 69(6):1061–1068.
- 496 [Curto et al., 2009] Curto, C., Sakata, S., Marguet, S., Itsikov, V., and Harris, K. D. (2009). A simple
497 model of cortical dynamics explains variability and state dependence of sensory responses in urethane-
498 anesthetized auditory cortex. *The Journal of Neuroscience*, 29(34):10600–10612.

- 499 [de la Rocha et al., 2007] de la Rocha, J., Doiron, B., Shea-Brown, E., Josić, K., and Reyes, A. (2007).
500 Correlation between neural spike trains increases with firing rate. *Nature*, 448(7155):802–806.
- 501 [Destexhe, 2009] Destexhe, A. (2009). Self-sustained asynchronous irregular states and Up-Down states
502 in thalamic, cortical and thalamocortical networks of nonlinear integrate-and-fire neurons. *Journal of*
503 *Computational Neuroscience*, 27(3):493–506.
- 504 [Ecker et al., 2014] Ecker, A. S., Berens, P., Cotton, R. J., Subramaniyan, M., Denfield, G. H., Cadwell,
505 C. R., Smirnakis, S. M., Bethge, M., and Tolias, A. S. (2014). State dependence of noise correlations in
506 macaque primary visual cortex. *Neuron*, 82(1):235–248.
- 507 [Ecker et al., 2010] Ecker, A. S., Berens, P., Keliris, G. a., Bethge, M., Logothetis, N. K., and Tolias, A. S.
508 (2010). Decorrelated neuronal firing in cortical microcircuits. *Science*, 327(5965):584–587.
- 509 [Erisken et al., 2014] Erisken, S., Vaicieliunaite, A., Jurjut, O., Fiorini, M., Katzner, S., Busse, L., Reichardt,
510 W., and Neuroscience, I. (2014). Article Effects of Locomotion Extend throughout the Mouse Early Visual
511 System. *Current Biology*, 24(24):1–9.
- 512 [Fino and Yuste, 2011] Fino, E. and Yuste, R. (2011). Dense inhibitory connectivity in neocortex. *Neuron*,
513 69(6):1188–1203.
- 514 [Garcia-Lazaro et al., 2013] Garcia-Lazaro, J. A., Belliveau, L. A., and Lesica, N. A. (2013). Independent
515 population coding of speech with sub-millisecond precision. *The Journal of Neuroscience*, 33(49):19362–
516 19372.
- 517 [Gentet et al., 2010] Gentet, L. J., Avermann, M., Matyas, F., Staiger, J. F., and Petersen, C. C. (2010).
518 Membrane potential dynamics of gabaergic neurons in the barrel cortex of behaving mice. *Neuron*,
519 65(3):422–435.
- 520 [Gentet et al., 2012] Gentet, L. J., Kremer, Y., Taniguchi, H., Huang, Z. J., Staiger, J. F., and Petersen,
521 C. C. (2012). Unique functional properties of somatostatin-expressing gabaergic neurons in mouse barrel
522 cortex. *Nature neuroscience*, 15(4):607–612.

- 523 [Goard and Dan, 2009] Goard, M. and Dan, Y. (2009). Basal forebrain activation enhances cortical coding
524 of natural scenes. *Nature Neuroscience*, 12(11):1444–1449.
- 525 [Goris et al., 2014] Goris, R. L. T., Movshon, J. A., and Simoncelli, E. P. (2014). Partitioning neuronal
526 variability. *Nature Neuroscience*, 17(6):858–65.
- 527 [Haider et al., 2013] Haider, B., Häusser, M., and Carandini, M. (2013). Inhibition dominates sensory re-
528 sponses in the awake cortex. *Nature*, 493(7430):97–100.
- 529 [Hansen et al., 2012] Hansen, B. J., Chelaru, M. I., and Dragoi, V. (2012). Correlated variability in laminar
530 cortical circuits. *Neuron*, 76(3):590–602.
- 531 [Harris and Thiele, 2011] Harris, K. D. and Thiele, A. (2011). Cortical state and attention. *Nature Reviews
532 Neuroscience*, 12(9):509–523.
- 533 [Hofer et al., 2011] Hofer, S. B., Ko, H., Pichler, B., Vogelstein, J., Ros, H., Zeng, H., Lein, E., Lesica, N. A.,
534 and Mrsic-Flogel, T. D. (2011). Differential connectivity and response dynamics of excitatory and inhibitory
535 neurons in visual cortex. *Nature Neuroscience*, 14(8):1045–1052.
- 536 [Isaacson and Scanziani, 2011] Isaacson, J. S. and Scanziani, M. (2011). How inhibition shapes cortical
537 activity. *Neuron*, 72(2):231–243.
- 538 [Jones, 2008] Jones, B. E. (2008). Modulation of cortical activation and behavioral arousal by cholinergic
539 and orexinergic systems. *Annals of the New York Academy of Sciences*, 1129:26–34.
- 540 [Kato et al., 2013] Kato, H. K., Gillet, S. N., Peters, A. J., Isaacson, J. S., and Komiyama, T. (2013).
541 Parvalbumin-expressing interneurons linearly control olfactory bulb output. *Neuron*, 80(5):1218–1231.
- 542 [Kuchibhotla et al., 2016] Kuchibhotla, K., Gill, J., Papadoyannis, E., Hindmarsh Sten, T., and Froemke, R.
543 (2016). A synaptic and circuit switch for control of flexible behavior. *Cosyne Abstracts 2016*.
- 544 [Latham et al., 2000] Latham, P. E., Richmond, B. J., Nelson, P. G., and Nirenberg, S. (2000). Intrinsic
545 dynamics in neuronal networks. I. Theory. *Journal of Neurophysiology*, 83(2):808–827.

- 546 [Lee et al., 2014] Lee, A. M., Hoy, J. L., Bonci, A., Wilbrecht, L., Stryker, M. P., and Niell, C. M. (2014).
547 Identification of a brainstem circuit regulating visual cortical state in parallel with locomotion. *Neuron*,
548 83(2):455–466.
- 549 [Lee et al., 2012] Lee, S.-H., Kwan, A. C., Zhang, S., Phoumthipphavong, V., Flannery, J. G., Masmanidis,
550 S. C., Taniguchi, H., Huang, Z. J., Zhang, F., Boyden, E. S., et al. (2012). Activation of specific interneurons
551 improves feature selectivity and visual perception. *Nature*, 488(7411):379–383.
- 552 [Litwin-Kumar and Doiron, 2012] Litwin-Kumar, A. and Doiron, B. (2012). Slow dynamics and high variability
553 in balanced cortical networks with clustered connections. *Nature Neuroscience*, 15(11):1498–1505.
- 554 [London et al., 2010] London, M., Roth, A., Beeren, L., Häusser, M., and Latham, P. E. (2010). Sensitivity to
555 perturbations *in vivo* implies high noise and suggests rate coding in cortex. *Nature*, 466(7302):123–127.
- 556 [Luczak et al., 2009] Luczak, A., Barthó, P., and Harris, K. D. (2009). Spontaneous events outline the realm
557 of possible sensory responses in neocortical populations. *Neuron*, 62(3):413–425.
- 558 [Macke et al., 2011] Macke, J. H., Buesing, L., Cunningham, J. P., Byron, M. Y., Shenoy, K. V., and Sahani,
559 M. (2011). Empirical models of spiking in neural populations. *Advances in Neural Information Processing
560 Systems*, pages 1350–1358.
- 561 [Madisen et al., 2012] Madisen, L., Mao, T., Koch, H., Zhuo, J.-m., Berenyi, A., Fujisawa, S., Hsu, Y.-W. A.,
562 Garcia III, A. J., Gu, X., Zanella, S., et al. (2012). A toolbox of cre-dependent optogenetic transgenic mice
563 for light-induced activation and silencing. *Nature Neuroscience*, 15(5):793–802.
- 564 [Marder et al., 2015] Marder, E., Goeritz, M. L., and Otopalik, A. G. (2015). Robust circuit rhythms in
565 small circuits arise from variable circuit components and mechanisms. *Current Opinion in Neurobiology*,
566 31:156–163.
- 567 [McGinley et al., 2015a] McGinley, M., David, S., and McCormick, D. (2015a). Cortical Membrane Potential
568 Signature of Optimal States for Sensory Signal Detection. *Neuron*, 87(1):179–192.

- 569 [McGinley et al., 2015b] McGinley, M. J., Vinck, M., Reimer, J., Batista-Brito, R., Zagha, E., Cadwell, C. R.,
570 Tolias, A. S., Cardin, J. A., and McCormick, D. A. (2015b). Waking state: rapid variations modulate neural
571 and behavioral responses. *Neuron*, 87(6):1143–1161.
- 572 [Mitchell et al., 2009] Mitchell, J. F., Sundberg, K. a., and Reynolds, J. H. (2009). Spatial Attention Decorre-
573 lates Intrinsic Activity Fluctuations in Macaque Area V4. *Neuron*, 63(6):879–888.
- 574 [Mochol et al., 2015] Mochol, G., Hermoso-Mendizabal, A., Sakata, S., Harris, K. D., and de la Rocha, J.
575 (2015). Stochastic transitions into silence cause noise correlations in cortical circuits. *Proceedings of the
576 National Academy of Sciences*, 112(11):201410509.
- 577 [Moreno-bote et al., 2014] Moreno-bote, R., Beck, J., Kanitscheider, I., Pitkow, X., Latham, P., and Pouget,
578 A. (2014). Information-limiting correlations. *Nature Neuroscience*, 17(10):1410–1417.
- 579 [Okun et al., 2015] Okun, M., Steinmetz, N. A., Cossell, L., Iacaruso, M. F., Ko, H., Barthó, P., Moore, T.,
580 Hofer, S. B., Mrsic-Flogel, T. D., Carandini, M., et al. (2015). Diverse coupling of neurons to populations
581 in sensory cortex. *Nature*, 521(7553):511–515.
- 582 [Otazu et al., 2009] Otazu, G. H., Tai, L.-H., Yang, Y., and Zador, A. M. (2009). Engaging in an auditory task
583 suppresses responses in auditory cortex. *Nature Neuroscience*, 12(5):646–654.
- 584 [Pachitariu et al., 2015] Pachitariu, M., Lyamzin, D. R., Sahani, M., and Lesica, N. A. (2015). State-
585 dependent population coding in primary auditory cortex. *The Journal of Neuroscience*, 35(5):2058–2073.
- 586 [Pachitariu et al., 2013] Pachitariu, M., Petreska, B., and Sahani, M. (2013). Recurrent linear models of
587 simultaneously-recorded neural populations. *Advances in Neural Information Processing Systems*, pages
588 3138–3146.
- 589 [Packer and Yuste, 2011] Packer, A. M. and Yuste, R. (2011). Dense, unspecific connectivity of neocortical
590 parvalbumin-positive interneurons: a canonical microcircuit for inhibition? *The Journal of Neuroscience*,
591 31(37):13260–13271.

- 592 [Polack et al., 2013] Polack, P.-O., Friedman, J., and Golshani, P. (2013). Cellular mechanisms of brain
593 state-dependent gain modulation in visual cortex. *Nature Neuroscience*, 16(9):1331–9.
- 594 [Renart et al., 2010] Renart, A., de la Rocha, J., Bartho, P., Hollender, L., Parga, N., Reyes, A., and Harris,
595 K. D. (2010). The asynchronous state in cortical circuits. *Science*, 327(5965):587–590.
- 596 [Roux and Buzsáki, 2015] Roux, L. and Buzsáki, G. (2015). Tasks for inhibitory interneurons in intact brain
597 circuits. *Neuropharmacology*, 88:10–23.
- 598 [Rubin et al., 2015] Rubin, D. B., Van Hooser, S. D., and Miller, K. D. (2015). The stabilized supralinear
599 network: A unifying circuit motif underlying multi-input integration in sensory cortex. *Neuron*, 85(2):402–
600 417.
- 601 [Sachidhanandam et al., 2013] Sachidhanandam, S., Sreenivasan, V., Kyriakatos, A., Kremer, Y., and Pe-
602 tersen, C. C. (2013). Membrane potential correlates of sensory perception in mouse barrel cortex. *Nature
603 neuroscience*, 16(11):1671–1677.
- 604 [Sakata, 2016] Sakata, S. (2016). State-dependent and cell type-specific temporal processing in auditory
605 thalamocortical circuit. *Scientific Reports*, 6.
- 606 [Sakata and Harris, 2009] Sakata, S. and Harris, K. D. (2009). Laminar structure of spontaneous and
607 sensory-evoked population activity in auditory cortex. *Neuron*, 64(3):404–418.
- 608 [Sakata and Harris, 2012] Sakata, S. and Harris, K. D. (2012). Laminar-dependent effects of cortical state
609 on auditory cortical spontaneous activity. *Frontiers in Neural Circuits*, 6(109):6.
- 610 [Schneider et al., 2014] Schneider, D. M., Nelson, A., and Mooney, R. (2014). A synaptic and circuit basis
611 for corollary discharge in the auditory cortex. *Nature*, 513(7517):189–194.
- 612 [Schölvinck et al., 2015] Schölvinck, M. L., Saleem, A. B., Benucci, A., Harris, K. D., and Carandini, M.
613 (2015). Cortical state determines global variability and correlations in visual cortex. *The Journal of
614 Neuroscience*, 35(1):170–178.

- 615 [Shadlen et al., 1996] Shadlen, M. N., Britten, K. H., Newsome, W. T., and Movshon, J. a. (1996). A computational analysis of the relationship between neuronal and behavioral responses to visual motion. *Journal of Neuroscience*, 16(4):1486–1510.
- 616
- 617
- 618 [Sippy and Yuste, 2013] Sippy, T. and Yuste, R. (2013). Decorrelating action of inhibition in neocortical networks. *The Journal of Neuroscience*, 33(23):9813–9830.
- 619
- 620 [Tan et al., 2014] Tan, A. Y. Y., Chen, Y., Scholl, B., Seidemann, E., and Priebe, N. J. (2014). Sensory stimulation shifts visual cortex from synchronous to asynchronous states. *Nature*, 509(7499):226–9.
- 621
- 622 [van Vreeswijk and Sompolinsky, 1996] van Vreeswijk, C. and Sompolinsky, H. (1996). Chaos in neuronal networks with balanced excitatory and inhibitory activity. *Science*, 274(5293):1724–1726.
- 623
- 624 [Vinck et al., 2015] Vinck, M., Batista-Brito, R., Knoblich, U., and Cardin, J. (2015). Arousal and Locomotion Make Distinct Contributions to Cortical Activity Patterns and Visual Encoding. *Neuron*, 86(3):740–754.
- 625
- 626 [Wilson et al., 2012] Wilson, N. R., Runyan, C. A., Wang, F. L., and Sur, M. (2012). Division and subtraction by distinct cortical inhibitory networks in vivo. *Nature*, 488(7411):343–348.
- 627
- 628 [Wolf et al., 2014] Wolf, F., Engelken, R., Puelma-Touzel, M., Weidinger, J. D. F., and Neef, A. (2014). Dynamical models of cortical circuits. *Current Opinion in Neurobiology*, 25:228–236.
- 629
- 630 [Yu et al., 2015] Yu, X., Ye, Z., Houston, C. M., Zecharia, A. Y., Ma, Y., Zhang, Z., Uygun, D. S., Parker, S., Vyssotski, A. L., Yustos, R., et al. (2015). Wakefulness is governed by gaba and histamine cotransmission. *Neuron*, 87(1):164–178.
- 631
- 632
- 633 [Zhou et al., 2014] Zhou, M., Liang, F., Xiong, X. R., Li, L., Li, H., Xiao, Z., Tao, H. W., and Zhang, L. I. (2014). Scaling down of balanced excitation and inhibition by active behavioral states in auditory cortex. *Nature neuroscience*, 17(6):841–850.
- 634
- 635
- 636 [Zhu et al., 2015] Zhu, Y., Qiao, W., Liu, K., Zhong, H., and Yao, H. (2015). Control of response reliability by parvalbumin-expressing interneurons in visual cortex. *Nature Communications*, 6.
- 637

638 **FIGURE CAPTIONS**

639 **Figure 1. Cortical networks exhibit a wide variety of intrinsic dynamics**

640 (A) Multi-neuron raster plots showing examples of a short segment of spontaneous activity from each of our
641 recording types. Each row in each plot represents the spiking of one single unit. Note that recordings made
642 under urethane were separated into two different recording types, synchronized (sync) and desynchronized
643 (desync), as described in the Methods.

644 (B) The autocorrelation function of the multi-unit activity (MUA, the summed spiking of all neurons in the
645 population in 15 ms time bins) for each example recording. The timescale of the autocorrelation function
646 (the autocorr decay) was measured by fitting an exponential function to its envelope as indicated.

647 (C) The values of the MUA across time bins sorted in ascending order. The percentage of time bins with
648 zero spikes (the % silence) is indicated.

649 (D) Scatter plots showing all possible pairwise combinations of the summary statistics for each recording.
650 Each point represents the values for one recording. Colors correspond to recording types as in A. The
651 recordings shown in A are denoted by open circles. The best fit line and the fraction of the variance that it
652 explained are indicated on each plot.

653 (E) The percent of the variance in the summary statistics across recordings that is explained by each prin-
654 cipal component of the values.

655 **Figure 2. A deterministic spiking network model of cortical activity**

656 (A) A schematic diagram of our deterministic spiking network model. An example of a short segment of the
657 intracellular voltage of a model neuron is also shown, along with the corresponding excitatory, inhibitory and
658 adaptation currents.

659 (B) An example of macroscopic variability in cortical recordings and network simulations. The top two multi-
660 neuron raster plots show spontaneous activity generated by the model. By adding a very small perturbation,
661 in this case one spike added to a single neuron, the subsequent activity patterns of the network can change
662 dramatically. The middle traces show the intracellular voltage of the model neuron to which the spike was
663 added. The bottom two raster plots show a similar phenomenon observed in vivo. Two segments of ac-
664 tivity extracted from different periods during the same recording were similar for three seconds, but then
665 immediately diverged.

666 (C) The autocorrelation function of the MUA measured from network simulations with different model pa-
667 rameter values. Each column shows the changes in the autocorrelation function as the value of one model
668 parameter is changed while all others are held fixed. The fixed values used were $w_I = 0.22$, $w_A = 0.80$,
669 $w_E = 4.50$, $b_1 = 0.03$, $b_0 = 0.013$.

670 (D) The summary statistics measured from network simulations with different model parameter values. Each
671 line shows the changes in the indicated summary statistic as one model parameter is changed while all
672 others are held fixed. Fixed values were as in C.

673 **Figure 3. Deterministic spiking networks reproduce the dynamics observed in vivo**

674 (A) A schematic diagram illustrating how the parameters of the network model were fit to individual multi-
675 neuron recordings.

676 (B) Examples of spontaneous activity from different recordings, along with spontaneous activity generated
677 by the model fit to each recording.

678 (C) The left column shows the autocorrelation function of the MUA for each recording, plotted as in Figure
679 1. The black lines show the autocorrelation function measured from spontaneous activity generated by the
680 model fit to each recording. The middle column shows the sorted MUA for each recording along with the
681 corresponding model fit. The right column shows the mean pairwise correlations between the spiking activity

682 of all pairs of neurons in each recording (after binning activity in 15 ms bins). The colored circles show the
683 correlations measured from the recordings and the black open circles show the correlations measured from
684 from spontaneous activity generated by the model fit to each recording.

685 **Figure 4. Deterministic spiking networks reproduce the noise correlations observed in vivo**

686 (A) Multi-neuron raster plots and PSTHs showing examples of evoked responses from each of our recording
687 types. Each row in each raster plot represents the spiking of one single unit. Each raster plot for each record-
688 ing type shows the response on a single trial. The PSTH shows the MUA averaged across all presentations
689 of the stimulus. Different stimuli were used for different recording types (see Methods).

690 (B) A scatter plot showing the mean spike rates and mean pairwise noise correlations (after binning the
691 evoked responses in 15 ms bins) for each recording. Each point represents the values for one recording.
692 Colors correspond to recording types as in A. The recordings shown in A are denoted by open circles.
693 Values are only shown for the 38 of 59 recordings that contained both spontaneous activity and evoked
694 responses.

695 (C) A schematic diagram illustrating the modelling of evoked responses.

696 (D) The top left plot shows the speech waveform presented in the IC recordings used as input to the model
697 cortical network. The top right plot shows PSTHs formed by averaging IC responses across all presentations
698 of speech and across all IC neurons in each preferred frequency group. The raster plots show the recorded
699 responses of two cortical populations to repeated presentations of speech, along with the activity generated
700 by the network model fit to each recording when driven by IC responses to the same speech.

701 (E) A scatter plot showing the noise correlations of speech responses measured from the actual recordings
702 and from simulations of the network model fit to each recording when driven by IC responses to speech.

703 **Figure 5. Strong inhibition suppresses noise correlations, enhances selectivity, and enables accu-**
704 **rate decoding**

705 (A) Scatter plots showing the mean pairwise noise correlations measured from simulations of the network
706 model fit to each recording when driven by IC responses to speech versus the value of the different model
707 parameters. Colors correspond to recording types as in Figure 4. The recordings shown in Figure 4D are
708 denoted by open circles.

709 (B) The mean pairwise noise correlations measured from network simulations with different values of the
710 inhibition parameter w_I . The values of all other parameters were held fixed at those fit to each recording.

711 Each line corresponds to one recording. Colors correspond to recording types as in Figure 4.

712 (C,E) Scatter plots showing tuning width and decoding error, plotted as in A.

713 (D,F) The tuning width and decoding error measured from network simulations with different values of the
714 inhibition parameter w_I , plotted as in B.

715 **Figure 6. Fast-spiking neurons are more active during periods of cortical desynchronization with**
716 **weak noise correlations**

717 (A) The cortical synchrony at different points during two recordings from V1 of awake mice, measured as
718 the log of the ratio of low-frequency (3 -10 Hz) LFP power to high-frequency (11 - 96 Hz). The distribution of
719 synchrony values across each recording is also shown. The lines indicate the median of each distribution.

720 (B) A scatter plot showing the noise correlations measured during trials in which the cortex was in either a
721 relatively synchronized (sync) or desynchronized (desync) state for each recording. Each point indicates the
722 mean pairwise correlations between the spiking activity of all pairs of neurons in one recording (after binning
723 the activity in 15 ms bins). Trials with the highest 50% of synchrony values were classified as sync and trials
724 with the lowest 50% of synchrony values were classified as desync. Values for 13 different recordings are

725 shown.

726 (C) A scatter plot showing noise correlations versus the mean synchrony for trials with the highest and lowest
727 50% of synchrony values for each recording. Colors indicate different recordings.

728 (D) Spectrograms showing the average LFP power during trials with the highest (sync) and lowest (desync)
729 20% of synchrony values across all recordings. The values shown are the deviation from the average
730 spectrogram computed over all trials.

731 (E) The average PSTHs of FS and RS neurons measured from evoked responses during trials with the
732 highest (sync) and lowest (desync) 20% of synchrony values across all recordings. The lines show the
733 mean across all cells, and the error bars indicate +/-1 SEM.

734 (F) The average spike rate of FS and RS neurons during the period from 0 to 500 ms following stimulus
735 onset, averaged across trials in each synchrony quintile. The lines show the mean across all cells, and the
736 error bars indicate +/-1 SEM.

737 (G) The cortical synchrony at different points during a urethane recording, plotted as in A. The line indicates
738 the value used to classify trials as synchronized (sync) or desynchronized (desync).

739 (H) A scatter plot showing the noise correlations measured during trials in which the cortex was in either a
740 synchronized (sync) or desynchronized (desync) state. Values for two different recordings are shown. Each
741 point for each recording shows the noise correlations measured from responses to a different speech token.

742 (I) Spectrograms showing the average LFP power during synchronized and desynchronized trials, plotted
743 as in D.

744 (J) The average PSTHs of FS and RS neurons during synchronized and desynchronized trials, plotted as in
745 E.

746 (K) The average spike rate of FS and regular-spiking RS neurons during the period from 0 to 500 ms

747 following stimulus onset during synchronized and desynchronized trials. The bars show the mean across all
748 cells, and the error bars indicate +/-1 SEM.

749 **Figure 7. Many fast-spiking neurons are silent under ketamine/xylazine anesthesia**

750 (A) The noise correlations measured from recordings of responses to speech in gerbil A1 under ketamine/xylazine
751 (KX) and fentanyl/mebetomidine/midazolam (FMM). Each point indicates the mean pairwise correlations be-
752 tween the spiking activity of all pairs of neurons in one recording (after binning the activity in 15 ms bins).

753 (B) The average PSTHs of FS and RS neurons under FMM or KX, plotted as in Figure 6.

754 (C) The average number of FS and regular-spiking RS neurons in recordings under FMM and KX. The bars
755 show the mean across all recordings, and the error bars indicate +/-1 SEM.

756 (D) The summed PSTHs of FS and RS neurons under FMM or KX, plotted as in Figure 6.

757 (E) The ratio of the total number of spikes from FS and RS neurons during the period from 0 to 500 ms
758 following stimulus onset. Each point shows the value for one recording.

759 **METHODS**

760 All of the recordings analyzed in this study have been described previously. Only a brief summary of the
761 relevant experimental details are provided here.

762 *Mouse V1*

763 The experimental details for the mouse V1 recordings have been previously described [Okun et al., 2015].
764 Briefly, mice were implanted with head plates under anaesthesia, and after a few days of recovery were
765 accustomed to having their head fixed while sitting or standing in a custom built tube. On the day of the
766 recording, the mice were briefly anaesthetised with isoflurane, and a small craniectomy above V1 was made.

767 Recordings were performed at least 1.5h after the animals recovered from the anaesthesia. Buzsaki32 or
768 A4x8 silicon probes were used to record the spiking activity of populations of neurons in the infragranular
769 layers of V1.

770 Visual stimuli were presented on two of the three available LCD monitors, positioned 25 cm from the animal
771 and covering a field of view of 120 60, extending in front and to the right of the animal. Visual stimuli
772 consisted of multiple presentations of natural movie video clips. For recordings of spontaneous activity, the
773 monitors showed a uniform grey background.

774 *Rat A1*

775 The experimental procedures for the rat A1 recordings have been previously described [Luczak et al., 2009].
776 Briefly, head posts were implanted on the skull of Sprague Dawley rats (300500 g) under ketaminexylazine
777 anesthesia, and a hole was drilled above the auditory cortex and covered with wax and dental acrylic. After
778 recovery, each animal was trained for 68 d to remain motionless in the restraining apparatus for increasing
779 periods (target, 12 h). On the day of the recording, each animal was briefly anesthetized with isoflurane
780 and the dura resected; after a 1 h recovery period, recording began. The recordings were made from
781 infragranular layers of auditory cortex with 32-channel silicon multi-tetrode arrays.

782 Sounds were delivered through a free-field speaker. As stimuli we used pure tones (3, 7, 12, 20, or 30 kHz
783 at 60 dB). Each stimulus had duration of 1s followed by 1s of silence.

784 *Gerbil A1*

785 The gerbil A1 recordings have been described in detail previously [Pachitariu et al., 2015]. Briefly, adult male
786 gerbils (70-90 g, P60-120) were anesthetized with one of three different anesthetics: ketamine/xylazine (KX),
787 fentanyl/meperidine/midazolam (FMM), or urethane. A small metal rod was mounted on the skull and
788 used to secure the head of the animal in a stereotaxic device in a sound-attenuated chamber. A craniotomy
789 was made over the primary auditory cortex, an incision was made in the dura mater, and a 32-channel
790 silicon multi-tetrode array was inserted into the brain. Only recordings from A1 were analyzed. Recordings

791 were made between 1 and 1.5 mm from the cortical surface (most likely in layer V).

792 Sounds were delivered to speakers coupled to tubes inserted into both ear canals for diotic sound presen-
793 tation along with microphones for calibration. Repeated presentations of a 2.5 s segment of human speech
794 were presented at a peak intensity of 75 dB SPL. For analyses of responses to different speech tokens,
795 seven 0.25 s segments were extracted from the responses to each 2.5 s segment.

796 *Gerbil IC*

797 The gerbil IC recordings have been described in detail previously [Garcia-Lazaro et al., 2013]. Recordings
798 were made under ketamine/xylazine anesthesia using a multi-tetrode array placed in the low-frequency
799 laminae of the central nucleus of the IC. Experimental details were otherwise identical to those for gerbil A1.
800 In addition to the human speech presented during the A1 recordings, tones with a duration of 75 ms and
801 frequencies between 256 Hz and 8192 Hz were presented at intensities between 55 and 85 dB SPL with a
802 75 ms pause between each presentation.

803 *Simulations*

We developed a network model using conductance-based quadratic integrate and fire neurons. There are three currents in the model: an excitatory, an inhibitory and an adaptation current. The subthreshold membrane potential for a single neuron i obeys the equation

$$\tau_m \frac{dV_i}{dt} = -(V_i - E_L) * (V_i - V_{th}) - g_{Ei}(V_i - E_E) - g_{Ii}(V_i - E_I) + -g_{Di}(V_i - E_D).$$

When $V > V_{th}$, a spike is recorded in the neuron and the neuron's voltage is reset to $V_{reset} = 0.9V_{th}$. For simplicity, we set $V_{th} = 1$ and the leak voltage $E_L = 0$. The excitatory voltage $E_E = 2V_{th}$ and $E_I = E_D = -0.5V_{th}$. Each of the conductances has a representative differential equation which is dependent on the

spiking of the neurons in the network at the previous time step, s_{t-1} . The excitatory conductance obeys

$$\tau_E \frac{d\mathbf{g}_E}{dt} = -\mathbf{g}_E + A\mathbf{s}_{t-1} + \mathbf{b}.$$

where A is the matrix of excitatory connectivity and \mathbf{b} is the vector of tonic inputs to the neurons. The matrix of connectivity is random with a probability of 5% for the network of 512 neurons and their connectivities are randomly chosen from a uniform distribution between 0 and w_E . The tonic inputs \mathbf{b} have a minimum value b_0 , which we call the tonic input baseline added to a random draw from an exponential distribution with mean b_1 , which we call the tonic input spread, such that for neuron i $\mathbf{b}(i) = b_0 + \text{exprnd}(b_1)$. The inhibitory conductance obeys

$$\tau_I \frac{d\mathbf{g}_I}{dt} = -\mathbf{g}_I + w_I * (\exp(\sum \mathbf{s}_{t-1} * c) - 1).$$

804 where c controls the gain of the inhibitory conductance.

The adaptation conductance obeys

$$\tau_A \frac{d\mathbf{g}_A}{dt} = -\mathbf{g}_A + w_A \mathbf{s}_{t-1}.$$

805 The simulations are numerically computed using Eulers method with a time-step of 0.75 ms (this was the
806 lock-out window used for spike-sorting the in vivo recordings). Each parameter set was simulated for 900
807 seconds. The timescales are set to $\tau_m = 20$ ms, $\tau_E = 5.10$ ms, $\tau_I = 3.75$ ms, $\tau_A = 375$ ms, and the inhibitory
808 non-linearity controlled by $c = 0.25$. The remaining five parameters (w_I , w_A , w_E , b_1 , and b_0) were fit to the
809 spontaneous activity from multi-neuron recordings using the techniques described below. Their ranges were
810 (0.01-0.4), (0.4-1.45), (2.50-5.00), (0.005-0.10), and (0.0001-0.05) respectively.

811 To illustrate the ability of the network to generate activity patterns with macroscopic variability, we simulated

812 spontaneous activity with a parameter set that produces up and down state dynamics. Figure 2A shows the
813 membrane potential of a single neuron in this simulation and its conductances at each time step. Figure
814 2B shows the model run twice with the same set of initial conditions and parameters, but with an additional
815 single spike inserted into the network on the second run (circled in green).

816 *Parameter sweep analysis*

817 Figure 2C and D summarize the effects of changing each parameter on the structure of the spontaneous
818 activity patterns generated by the model. We held the values for all but one parameter fixed and swept
819 the other parameters values over the range in which network responses were not diverging and the network
820 was not completely silent. The fixed parameter values were set to approximately the median values obtained
821 from fits to all in vivo recordings. A similar parameter sweep analysis was performed in Figure 5 B, D, and
822 F. For this analysis, only inhibition was varied and the other parameter values were fixed as those fit to each
823 individual recording.

824 *GPU implementation*

825 We accelerated the network simulations by programming them on graphics processing units (GPUs) such
826 that we were able to run them at 650x real time with 15 networks running concurrently on the same GPU.
827 We were thus able to simulate \approx 10000 seconds of simulation time in 1 second of real time. To achieve this
828 acceleration, we took advantage of the large memory bandwidth of the GPUs. For networks of 512 neurons,
829 the state of the network (spikes, conductances and membrane potentials) can be stored in the very fast
830 shared memory available on each multiprocessor inside a GPU. A separate network was simulated on each
831 of the 8 or 15 multiprocessors available (video cards were GTX 690 or Titan Black). Low-level CUDA code
832 was interfaced with Matlab via mex routines.

833 *Summary statistics*

834 Several statistics of spikes were used to summarize the activity patterns observed in the in vivo recordings
835 and in the network simulations. Because there were on the order of 50 neurons in each recording, all of

836 the statistics below were influenced by small sample effects. To replicate this bias in the analysis of network
837 simulations, we subsampled 50 neurons from the network randomly and computed the same statistics we
838 computed from the in vivo recordings.

839 The noise correlations between each pair of cells in each population were measured from responses to
840 speech. The response of each cell to each trial was represented as a binary vector with 15 ms time bins.
841 The total correlation for each pair of cells was obtained by computing the correlation coefficient between the
842 actual responses. The signal correlation was computed after shuffling the order of repeated trials for each
843 time bin. The noise correlation was obtained by subtracting the signal correlation from the total correlation.

844 The multi-unit activity (MUA) was computed as the sum of spikes in all neurons in bins of 15 ms.

The autocorrelation function of the MUA at time-lag τ was computed from the formula

$$\text{ACF}(\tau) = \frac{1}{N_{samples}} \sum \text{MUA}(t) * \text{MUA}(t + \tau)$$

To measure the autocorrelation timescale, we fit one side of the ACF with a parametric function

$$\text{ACF}(\tau) \sim A \exp(-\tau/T) \cdot \cos(\tau/(2\pi t_{\text{period}}))$$

845 where A is an overall amplitude, T is a decay timescale and t_{period} is the oscillation period of the autocor-
846 relation function. There was not always a significant oscillatory component in the ACF, but the timescale of
847 decay accurately captured the duration over which the MUA was significantly correlated.

848 *Parameter searches*

849 To find the best fit parameters for each individual recording, we tried to find the set of model parameters for
850 which the in vivo activity and the network simulations had the same statistics. We measured goodness of fit
851 for each of the three statistics: pairwise correlations, the MUA distribution, the MUA ACF. Each statistic was

852 normalized appropriately to order 1, and the three numbers obtained were averaged to obtain an overall
853 goodness of fit.

The distance measure D_c between the mean correlations c_θ obtained from a set of parameters θ and the mean correlations c_n in dataset n was simply the squared error $D_c(c_n, c_\theta) = (c_n - c_\theta)^2$. This was normalized by the variance of the mean correlations across datasets to obtain the normalized correlation cost Cost_c , where $\langle x_n \rangle_n$ is used to denote the average of a variable x over datasets indexed by n .

$$\text{Cost}_c = \frac{D_c(c_n, c_\theta)}{\langle D_c(c_n, c_n) \rangle}$$

The distance measure D_m for the MUA distribution was the squared difference summed over the order rank bins k of the distribution $D_m(\text{MUA}_n, \text{MUA}_\theta) = \sum_k (\text{MUA}_n(k) - \text{MUA}_\theta(k))^2$. This was normalized by the distance between the data MUA and the mean data MUA. In other words, the cost measures how much closer the simulation is to the data distribution than the average of all data distributions.

$$\text{Cost}_m = \frac{D_m(\text{MUA}_n, \text{MUA}_\theta)}{D_m(\text{MUA}_n, \langle \text{MUA}_n \rangle)}$$

Finally, the distance measure D_a for the autocorrelation function of the MUA was the squared difference summed over time lag bins t of the distribution $D_a(\text{ACF}_n, \text{ACF}_\theta) = \sum_t (\text{ACF}_n(t) - \text{ACF}_\theta(t))^2$. This was normalized by the distance between the data ACF and the mean data ACF.

$$\text{Cost}_a = \frac{D_a(\text{ACF}_n, \text{ACF}_\theta)}{D_a(\text{ACF}_n, \langle \text{ACF}_n \rangle)}$$

854 The total cost of parameters θ on dataset n is therefore $\text{Cost}(n, \theta) = \text{Cost}_c + \text{Cost}_m + \text{Cost}_a$. Approximately
855 two million networks were simulated on a grid of parameters for 600 seconds each of spontaneous activity,
856 and their summary statistics (c_θ , MUA $_\theta$ and ACF $_\theta$) were retained. The Cost was smoothed for each dataset
857 by averaging with the nearest 10 other simulations on the grid. This ensured that some of the sampling noise

858 was removed and parameters were estimated more robustly. The best fit set of parameters was chosen as
859 the minimizer of this smoothed cost function, on a dataset by dataset basis.

860 *Stimulus-driven activity*

861 Once the simulated networks were fit to the spontaneous neuronal activity, we drove them with an external
862 input to study their evoked responses. The stimulus was either human speech (as presented during our
863 gerbil A1 recordings) or pure tones. The external input to the network was constructed using recordings
864 from 563 neurons from the inferior colliculus (IC). For all recordings in the IC the mean pairwise noise
865 correlations were near-zero and the Fano Factors of individual neurons were close to 1 [Belliveau et al.,
866 2014], suggesting that responses of IC neurons on a trial-by-trial basis are fully determined by the stimulus
867 alone, up to Poisson-like variability. Hence, we averaged the responses of IC neurons over trials and drove
868 the cortical network with this trial-averaged IC activity. We binned IC neurons by their preferred frequency in
869 response to pure tones, and drove each model cortical neuron with a randomly chosen subset of 10 neurons
870 from the same preferred-frequency bin. We rescaled the IC activity so that the input to the network had a
871 mean value of 0.06 and a maximum value of 0.32, which was three times greater than the average tonic
872 input.

We kept the model parameters fixed at the values fit to spontaneous activity and drove the network with 330 repeated presentations of the stimulus. We then calculated the statistics of the evoked activity. Noise correlations were measured in 15-ms bins as the residual correlations left after subtracting the mean response of each neuron to the stimulus across trials:

$$c_{ij} = \frac{1}{N_{samples}} \sum_t (s_i(t) - \langle s_i(t) \rangle)(s_j(t) - \langle s_j(t) \rangle)$$

873 where $s_i(t)$ is the summed spikes of neuron i in a 15-ms bin and $\langle s_i(t) \rangle$ is the mean response of neuron
874 i to the stimulus. The noise correlation value given for each recording is the mean of c_{ij} .

875 *Tuning width*

876 To determine tuning width to sound frequency, we used responses of IC neurons to single tones as inputs to
877 the model network. The connections from IC to the network were the same as described in the previous sec-
878 tion. Because the connectivity was tonotopic and IC responses are strongly frequency tuned, the neurons
879 in the model network inherited the frequency tuning. We did not model the degree of tonotopic fan-out of
880 connections from IC to cortex and, as a result, the tuning curves of the model neurons were narrow relative
881 to those observed in cortical recordings ???. We chose the full width of the tuning curve at half-max as a
882 standard measure of tuning width.

883 *Decoding tasks*

884 We computed decoding error for a classification task in which the single-trial activity of all model neurons
885 was used to infer which of seven different speech tokens was presented. The classifier was built on training
886 data using a linear discriminant formulation in which the Gaussian noise term was replaced by Poisson
887 likelihoods. Specifically, the activity of a neuron for each 15-ms bin during the response to each token was
888 fit as a Poisson distribution with the empirically-observed mean. To decode the response to a test trial, the
889 likelihood of each candidate token was computed and the token with the highest likelihood was assigned as
890 the decoded class. This classifier was chosen because it is very fast and can be used to model Poisson-like
891 variables, but we also verified that it produced decoding performance as good as or better than classical
892 high-performance classifiers like support vector machines.

893 *Classifying FS and RS cells*

894 We classified fast-spiking and regular-spiking cells based on their spike shape [Okun et al., 2015]. We
895 determined the trough-to-peak time of the mean spike waveform after smoothing with a gaussian kernel of
896 $\sigma = 0.5$ samples. The distribution of the trough-to-peak time τ was clearly bimodal in all types of recordings.
897 Following [Okun et al., 2015] we classified FS neurons in the awake data with $\tau < 0.6ms$ and RS neurons
898 with $\tau > 0.8ms$. The distributions of τ in the anesthetized data, although bimodal, did not have a clear

899 separation point, so we conservatively required $\tau < 0.4\text{ms}$ to classify an FS cell in these datasets and
900 $\tau > 0.65\text{ms}$ to classify RS cells (see Figure S4). The rest of the cells were not considered for the plots in
901 Figures 7 and 8 and are shown in gray on the histogram in Figure S4.

902 *Local field potential*

903 The low-frequency potential (LFP) was computed by low-pass filtering the raw signal with a cutoff of 300 Hz.
904 Spectrograms with adaptive time-frequency resolution were obtained by filtering the LFP with Hamming-
905 windowed sine and cosine waves and the spectral power was estimated as the sum of their squared ampli-
906 tudes. The length of the Hamming-window was designed to include two full periods of the sine and cosine
907 function at the respective frequency, except for frequencies of 1 Hz and above 30 Hz, where the window
908 length was clipped to a single period of the sine function at 1 Hz and two periods of the sine function at 30
909 Hz respectively. The synchrony level was measured as the log of the ratio of the low to high frequency power
910 (respective bands: 3-10 Hz and 11-96 Hz, excluding 45-55 Hz to avoid the line noise). We did not observe
911 significant gamma power peaks except for the line noise, in either the awake or anesthetized recordings.

912 *Dividing trials by synchrony*

913 We computed a synchrony value for each trial in the 500-ms window following stimulus onset. For Urethane
914 recordings, the values had a clear bimodal distribution and we separated the top and bottom of these
915 distributions into synchronized and desynchronized trials respectively. For awake recordings, the synchrony
916 index was not clearly bimodal, but varied across a continuum of relatively synchronized and desynchronized
917 states. To examine the effect of synchrony on noise correlations, we sorted all trials by their synchrony value,
918 classified the 50% of trials with the lowest values as desynchronized and the 50% of trials with the highest
919 values as synchronized, and computed the noise correlations for each set of trials for each recording. To
920 examine the effect of synchrony on FS and RS activity, we pooled all trials from all recordings, divided them
921 into quintiles by their synchrony value, and computed the average spike rates of FS and RS neurons for
922 each set of trials. For figures 7 and 8, noise correlations were computed aligned to the stimulus onsets in

923 windows of 500ms, to match the window used for measuring FS and RS activity as well as LFP power.

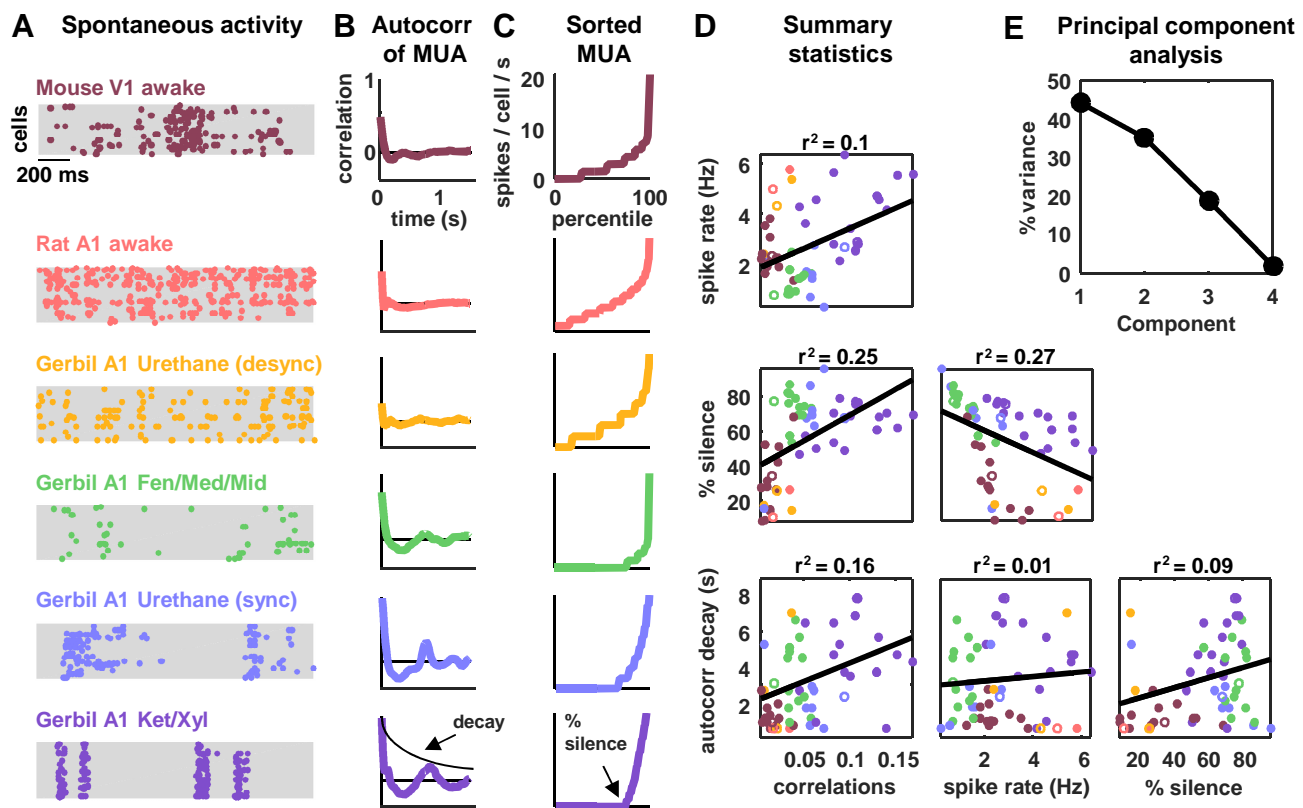


Figure 1

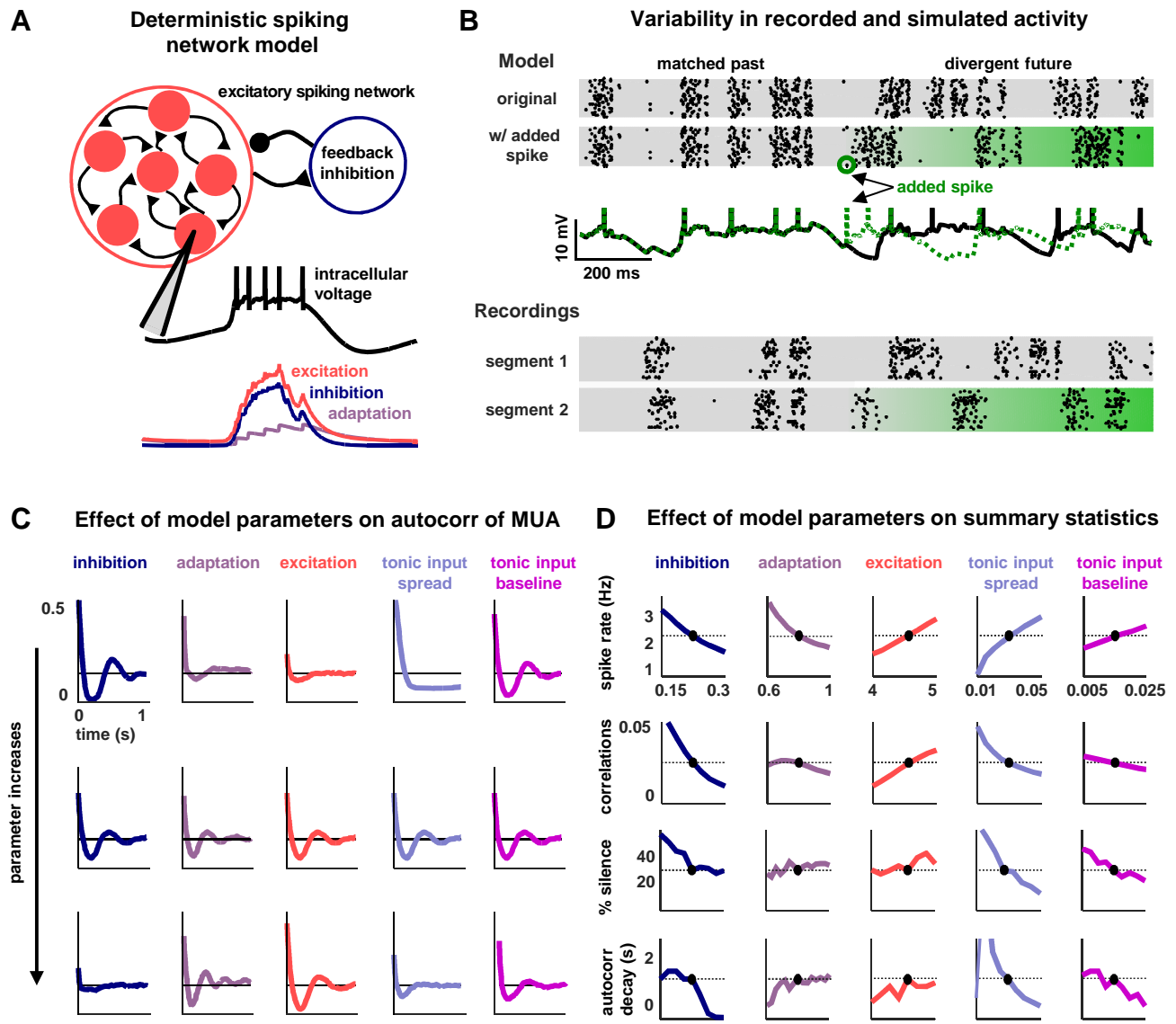
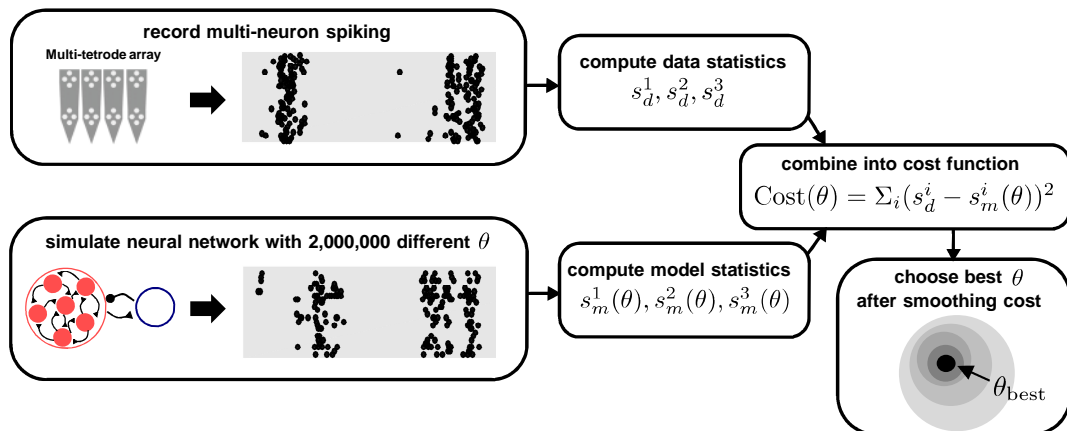


Figure 2

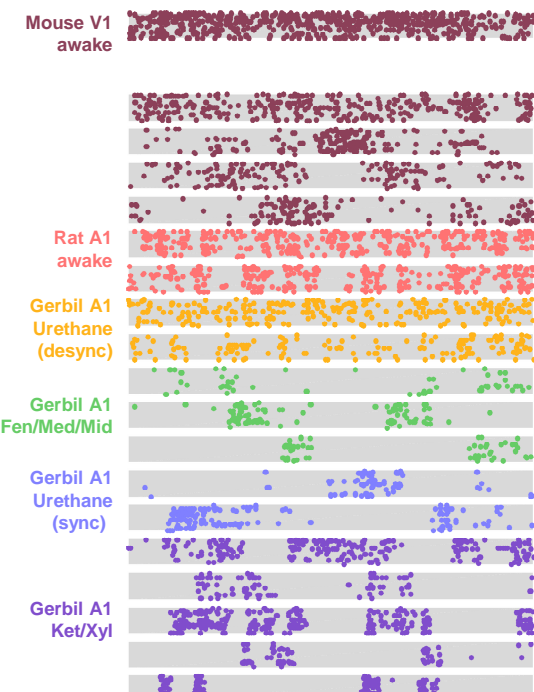
A

Fitting the model to individual multi-neuron recordings

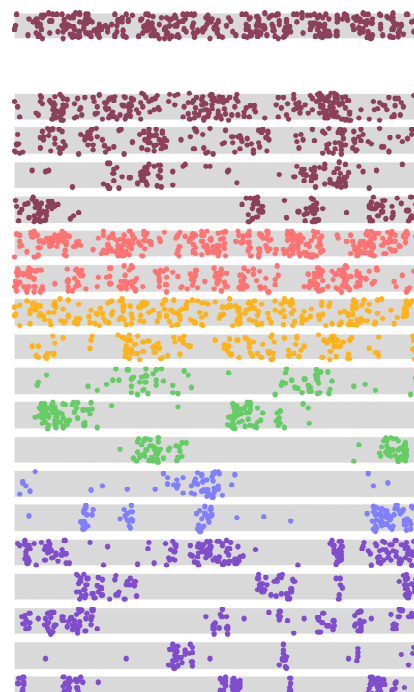


B

Recordings



Model



C Autocorr of MUA

Sorted MUA

Pairwise corr

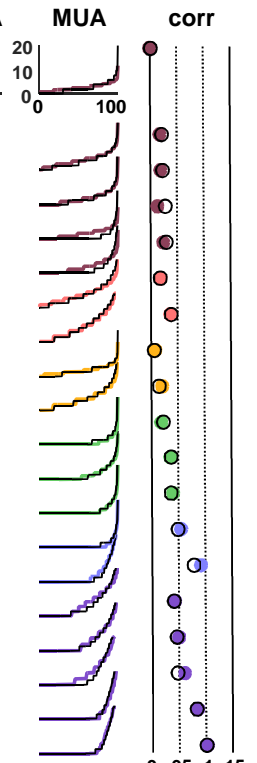


Figure 3

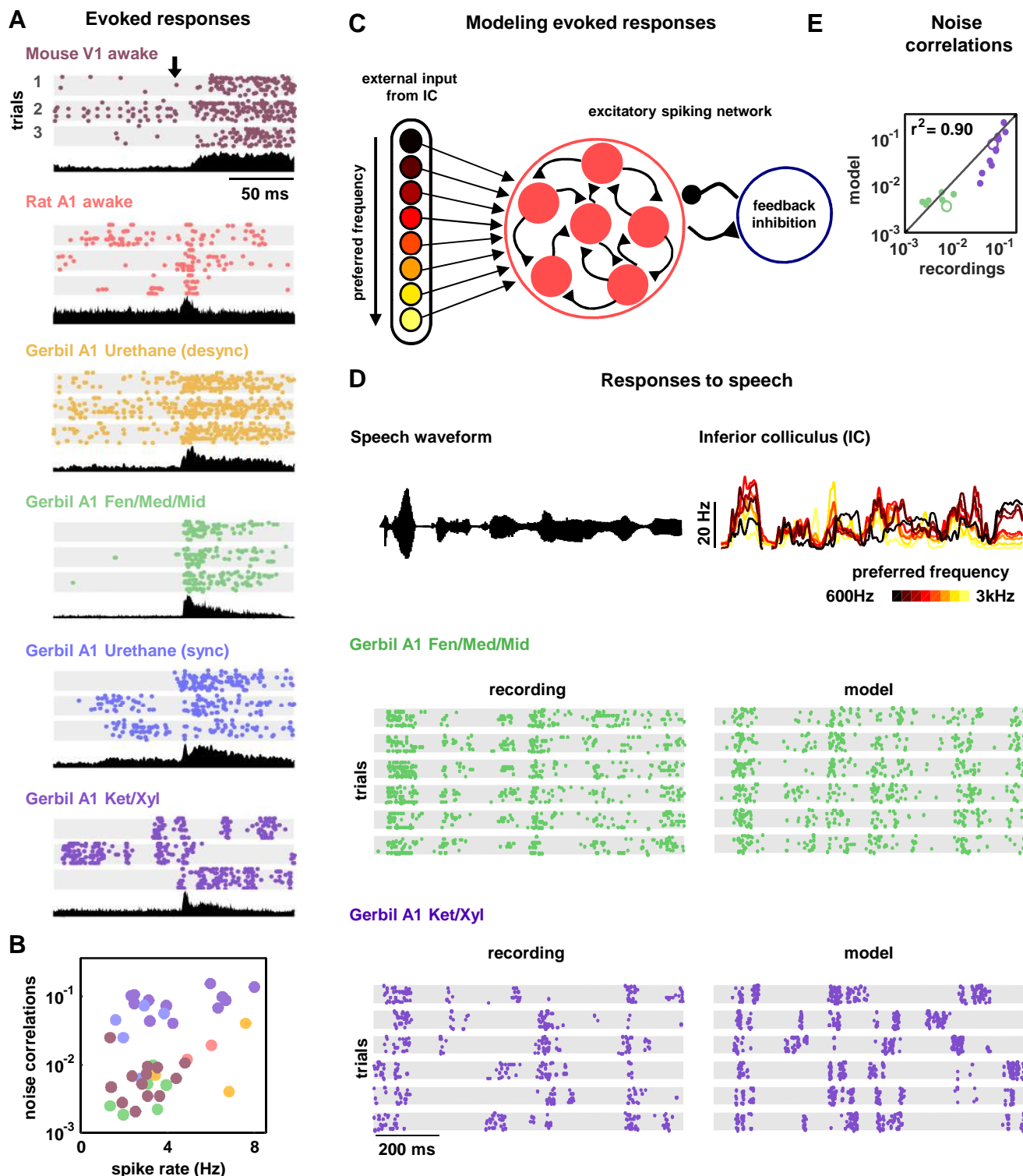


Figure 4

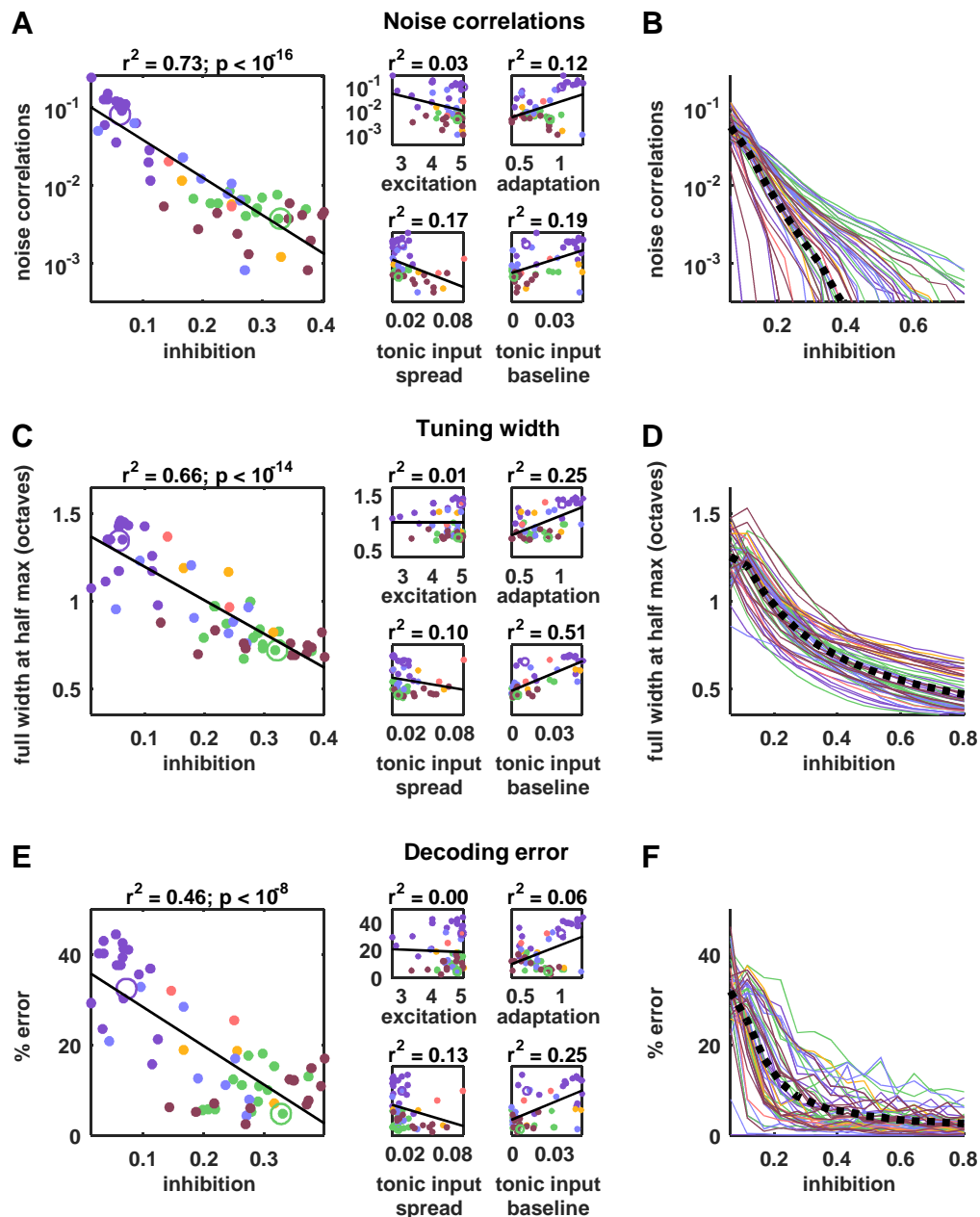


Figure 5

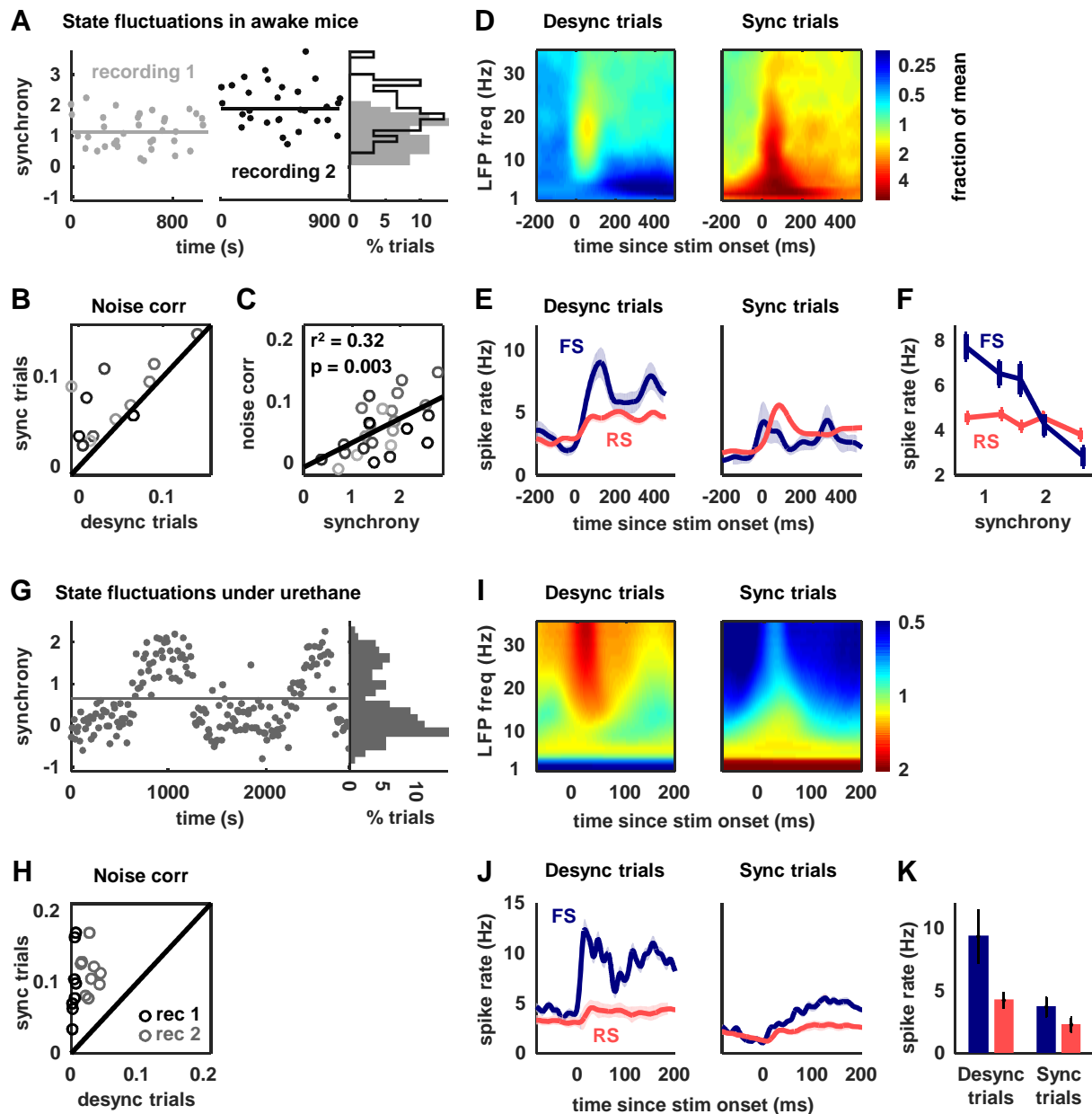


Figure 6

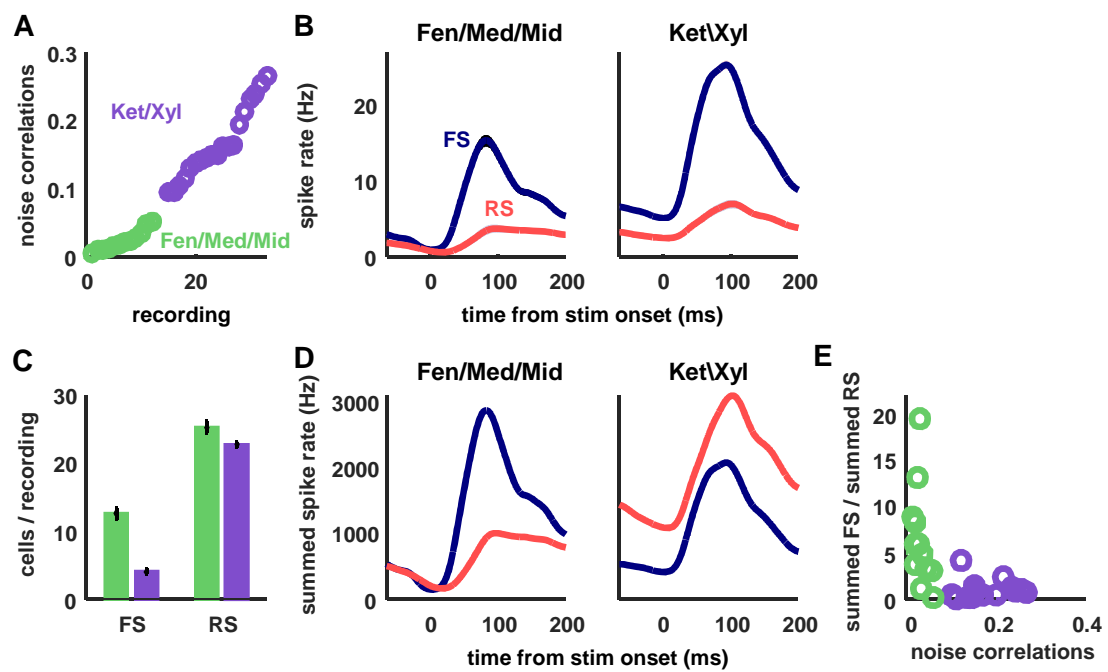


Figure 7